Pressure-driven Membrane Desalination

Weifan Liu[a], Joshua L. Livingston[a], Li Wang[b], Zhangxin Wang[c, d], Martina del Cerro[e],
Saad A. Younssi[f], Razi Epsztein[g], Menachem Elimelech* [e], and Shihong Lin* [a, h]

[a] Department of Civil and Environmental Engineering, Vanderbilt University, Nashville, Tennessee 37235-1831, USA
[b] State Key Laboratory of Pollution Control and Resource Reuse, Shanghai Institute of Pollution Control and Ecological Security, Tongji Advanced Membrane Technology Center, School of Environmental Science and Engineering, Tongji University, Shanghai 200092, China
[c] School of Ecology, Environment and Resources, Guangdong University of Technology, Guangzhou, Guangdong 510006, China
[d] Southern Marine Science and Engineering Guangdong Laboratory (Guangzhou), Guangzhou 511458, China
[e] Department of Chemical and Environmental Engineering, Yale University, New Haven, CT, 06520-8286, USA
[f] Laboratory of Materials, Membranes and Environment, Faculty of Sciences and Technologies, Hassan II University of Casablanca, P.O. Box 146, Mohammedia 20650, Morocco
[g] Faculty of Civil and Environmental Engineering, Technion − Israel Institute of Technology, Haifa 32000, Israel
[h] Department of Chemical and Bimolecular Engineering, Vanderbilt University, Nashville, Tennessee 37235-1831, USA

*Email:
Menachem Elimelech, menachem.elimelech@yale.edu;
Shihong Lin, shihing.lin@vanderbilt.edu

Abstract

Pressure-driven membrane desalination (PMD), such as reverse osmosis (RO) or nanofiltration (NF), has become an energy-efficient technology to address water shortage by tapping into saline waters to augment freshwater supply. This Primer describes several key methodological aspects of PMD, including membrane fabrication, characterization, and performance evaluation, system modeling, as well as process configurations and applications. State-of-the-art RO and NF membranes are thin-film composite polyamide (TFC-PA) membranes, which is the focus of our discussion on membrane development. We first describe the fabrication of TFC-PA membranes using interfacial polymerization and alternative methods. We then discuss the techniques for characterizing the morphological, structural, and interfacial properties of TFC-PA membranes, followed by a discussion on the experimental procedures and model frameworks for evaluating membrane performance. Certain caveats in data collection, interpretation, and reproducibility are discussed with best practices recommended. Additionally, we also introduce the general method for modeling module-scale behavior of PMD processes and discuss the process configurations along with existing and emerging applications of PMD. Finally, we provide an outlook for the development of PMD, highlighting the most meaningful directions for future research to further advance PMD beyond the state of the art.

[H1] Introduction

Pressure-driven membrane desalination (PMD) with reverse osmosis **[G]** (RO) has been at the cutting edge of freshwater production from saline waters for decades[1]. The breakthrough of this process occurred in the early 1960s with the invention of the first asymmetric cellulose acetate RO membrane by Loeb and Sourirajan[2]. The semi-permeable membrane with a thin active layer enabled the production of desalted water at high water flux under practical pressures, leading to successful implementation of RO at scale. The introduction of the thin-film composite polyamide (TFC-PA) membrane in the late 1970s[3,4] and the continuous improvements in the process engineering over the following decades (e.g., installation of energy recovery devices, EDR, and high-efficiency pumps) have further boosted the preeminence of RO over other seawater desalination technologies[1]. Beyond seawater RO (SWRO), the desalination of brackish water and municipal wastewater with lower salinity has also become practical using brackish water RO (BWRO) or nanofiltration **[G]** (NF), which utilize similar salt-rejecting membranes with looser structure that enables higher water flux at the cost of lower salt rejection[5].

The fundamental principle of PMD can be described as follows. To induce water flow from the high-salinity feed water to the low-salinity product water against the natural direction of water osmosis, the hydraulic pressure difference applied over the membrane must exceed osmotic pressure difference across the membrane[6]. Excess pressure beyond the osmotic pressure difference is applied to provide driving force for finite water flux and to overcome resistances to water flow through the membrane pores, which induces irreversible loses or generates entropy[1]. The applied hydraulic pressure (up to 80 bar for SWRO but lower for BWRO and NF) depends on feed salinity, the water recovery (WR) ratio, membrane permeability, and other operating and system design parameters[7]. Notably, the irreversible losses or entropy generation in RO are substantially lower than that in traditional thermal desalination techniques based on evaporation, rendering RO a highly energy-efficient approach for seawater desalination with a total energy consumption much closer to the thermodynamic limit (i.e., Gibbs free energy of separation) than thermal desalination[8,9].

Accounting for the largest share of globally desalinated water, state-of-the-art RO desalination still faces challenges that limit broader applications and stimulate extensive research. One noticeable example is the low rejection of neutral solutes (e.g., boron and specific micropollutants) by current RO membranes, which requires the introduction of an additional RO pass in some applications, thus increasing the capital and operational cost[10]. Other examples include the detrimental sensitivity of PA RO membranes to chlorine[11], decline of water flux over time due to membrane fouling and scaling[12], and brine management[13]. Ongoing research is therefore directed to address these shortcomings by exploring new membrane materials[14,15] and process designs[16,17].

In addition to the applied research to improve the performance of current PMD systems, fundamental studies to elucidate molecular transport phenomena in RO/NF membranes have been a major scientific pillar of the membrane research field[18]. Water and solute transport in RO/NF membranes have remained the center of theoretical study over the years, promoting the development of several mathematical models to describe mass transfer **[G]** in these membranes[19]. Most notably, the solution-diffusion model, describing water and solute transport as a two-step process of molecular partition into the membrane and the subsequent diffusion through the membrane, has prevailed in the membrane community for many years due to its simplicity and ability to explain certain major trends in membrane performance[20]. More recently, with additional experimental evidence, progress in molecular simulations, and development of experimental techniques with higher spatial and temporal resolution to study the kinetics of molecular transport through the membrane pore[21–23], updated models and theories for mass transport in RO membranes have been proposed[24–26]. Such exploration of fundamental transport phenomena in RO has promoted the collaboration between membrane scientists and researchers from other fields[22,27,28].

Observing the success of RO over the past 60 years for revolutionizing water desalination, this Primer overviews state-of-the-art methodologies and applications of PMD with RO and NF. We first introduce standard methods to fabricate, characterize, and test RO/NF membranes. Next, we discuss established approaches to analyze results from membrane characterization and interpret data from membrane performance tests using existing and recent transport models applied to both coupon and module scale systems. We also introduce and discuss traditional and emerging applications of PMD, highlighting current limitations of the method and challenges associated with reproducibility and data deposition. We conclude with an outlook to summarize the challenges and opportunities of PMD that require future research to address.

[H1] Experimentation

[H2] Membrane fabrication

State-of-the-art RO or NF membranes are TFC-PA membranes comprising an ultrathin, salt-rejecting PA active layer prepared atop a microporous support that provides mechanical integrity against applied pressure (**Fig. 1a**)[29]. The standard approach to fabricate TFC-PA membranes in industry is based on a process called interfacial polymerization **[G]** (IP), where a PA layer form via a self-inhibiting polycondensation reaction occurring at a water-organic solvent interface (**Fig. 1b**)[4,30–32]. Specifically, a microporous polysulfone (PS) or polyethersulfone (PES) support impregnated with an aqueous solution of amine monomers is exposed to an organic solvent solution of acyl chloride. The amine monomer is typically m-phenylenediamine (MPD) for making SWRO membranes and piperazine (PIP) for making NF membranes, whereas trimesoyl chloride (TMC) is often used as the acyl chloride with hexane as the organic solvent (**Fig. 1c**)[14]. It is believed that the amine monomers diffuse across the water-hexane interface to react with TMC in the hexane phase near the interface, forming a thin and crosslinked PA layer anchored to the microporous support[33]. The PA layer is typically less than 100 nm because its formation creates a barrier for the further encounter of amine and acyl chloride molecules for continuous polycondensation reaction, thus rendering the IP process “self-inhibiting”[30,34].

The morphology and performance of the TFC-PA is influenced by multiple factors in the IP process, including but not limited to, monomer species and solvent type (note that mixture of monomers or solvents can also be used)[35–38], the introduction of various additives (e.g., surfactants, organic molecules, salts, and nanoparticles)[39–42], the support layer structure[43,44], water chemistry of the amine solution[45], the use of interlayers[44,46], and the environmental conditions in the IP and/or post-treatment (annealing) process[38]. Detailed impacts of these factors on the morphology and performance of TFC-PA can be found in several recent reviews[31,47–50]. Despite decades of research that generates a large body of knowledge on practical ways to improve performance of TFC-PA membranes, mechanistic understanding of the details of PA layer formation remains insufficient.

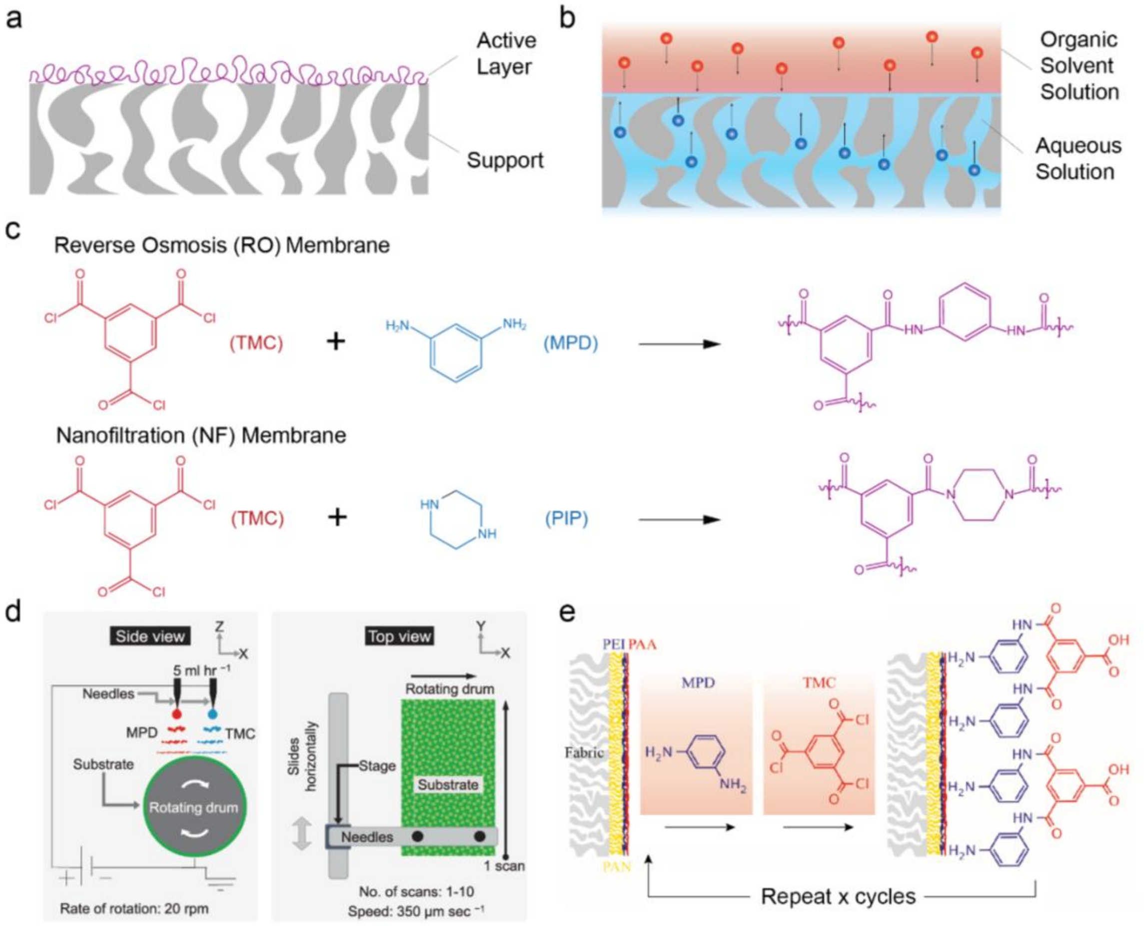

Fig. 1 | **Membrane fabrication methods. a.** Structure of the thin-film composite polyamide (TFC-PA) membrane. **b.** Interfacial polymerization occurring at the interface between an organic solvent solution of acid chlorides and an aqueous solution of amines. **c.** The polycondensation reaction of trimesoyl chloride (TMC) with m-phenylenediamine (MPD, for making reverse osmosis (RO) membranes) or piperazine (PIP, for making nanofiltration (NF) membranes). **d.** Schematic of TFC-PA membrane fabrication using electrospray-based additive manufacturing. e. Layer-by-layer deposition of reactive monomers to form TFC membranes. Figure d and figure e are adapted with permission from ref. 51 and ref. 58, respectively.

Beyond TFC-PA fabricated using the IP process, recent studies have explored the approach of additive manufacturing to make TFC-PA membrane by sequential deposition of amines and acyl chlorides using electrospray (**Fig. 1d**)[51,52]. Advantages of this additive approach for membrane fabrication include the formation of smooth PA layers with controllable film thickness, possibly more controllable microstructure[53], more efficient utilization of monomers, saving in solvents, and the possibility of adopting new polymer chemistries alternative to polyamide[51,54]. As a relatively new approach, however, electrospray method has not produced TFC-PA membranes with better performance than those fabricated using the state-of-the-art IP processes. Another extensively investigated method of fabricating RO and NF membranes is layer-by-layer deposition of molecules (polyelectrolytes or reactive monomers) on a substrate to form TFC membranes (**Fig. 1e**)[55–58]. Despite the advantage of having a rich selection of polymer chemistry to control membrane properties, membranes made via layer-by-layer deposition have not been applied for desalination at an industrial scale due to the inability to achieve ultrahigh salt rejection and slow speed of the layer-by-layer deposition approach as compared to the very fast IP process[59]. Due to the dominance of TFC-PA membranes in practical desalination applications, the following discussion will focus on TFC-PA membranes formed via IP, although most of the methods for characterization, performance testing, and modeling apply regardless of the specific material chemistry and fabrication method.

[H2] Membrane characterization

The physicochemical properties of a TFC-PA membrane have strong impacts on its desalination performance and are thus extensively characterized in many studies focusing on membrane fabrication. In general, a TFC-PA membrane is characterized for its morphology and structure, chemical composition, and interfacial properties, which will be discussed below.

[H3] Morphology and structure.

Three types of microscopic techniques are commonly used to characterize the morphology of TFC-PA membranes (**Fig. 2**), including scanning electron microscopy (SEM), transmission electron microscopy (TEM), and atomic force microscopy (AFM). SEM micrographs provide direct visualization of the surface (top-view) and cross-sectional morphology[60]. For example, TFC-PA membranes made using MPD amine monomers (for SWRO) have been shown to have ridge-and-valley morphology for the PA layer[60,61], whereas those fabricated using PIP amine monomers (for NF) typically have nodular morphology[62,63](**Fig. 2a**). Other interesting morphologies, such as stripes[39,62], craters[64,65], and 2D fractals[40], can also emerge with IP processes modified with additives or post-treatment. TEM is mostly performed to image the cross-section of TFC-PA membranes for evaluating the PA layer thickness and identifying voids in the PA layer by distinguishing different parts (the PA layer, the PS/PES support, and voids) based on their difference in electron transmittance (**Fig. 2a**). The interface of the PA layer and the PS/PES support can be more clearly discerned by increasing their contrast in electron transmission via staining the PA layer with heavy metals[66], or using elemental mapping based on energy dispersive X-ray spectroscopy (EDS) in scanning transmission electron microscopy (STEM)[59]. With metal staining or elemental mapping, the cross-sectional TEM micrographs can provide clear distinction between the PA and the microporous support layer (**Fig. 2b, 2c**) [66,67].

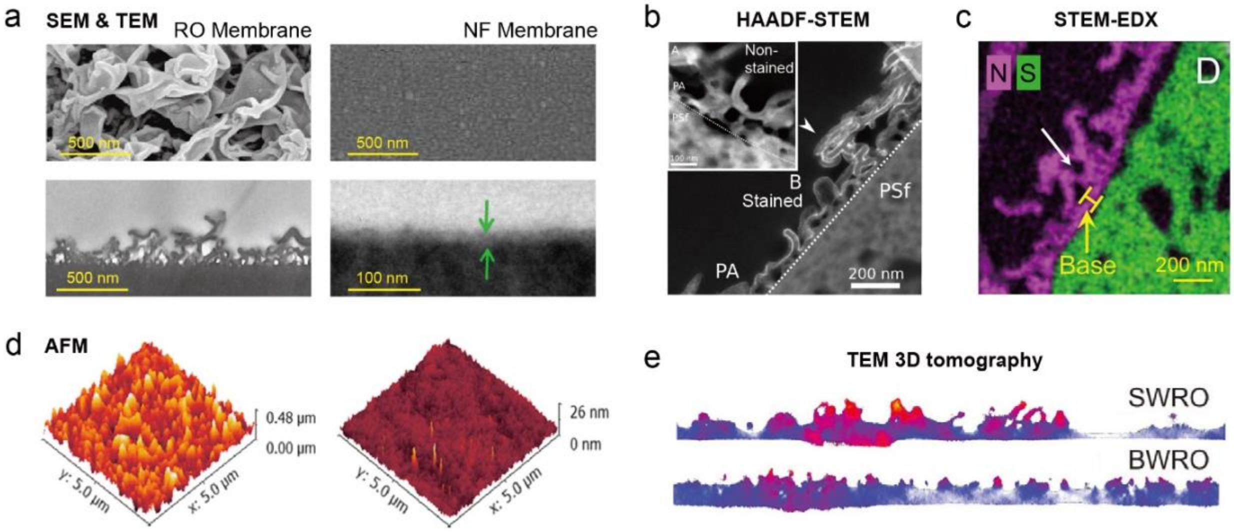

Fig. 2 | **Advanced imaging characterization results of TFC-PA membranes. a.** Scanning electron microscopy (SEM, top) and Transmission electron microscopy (TEM, bottom) images for RO and NF membranes. RO PA membrane has the clear "ridge and valley" structure. **b.** High-angle annular dark-field scanning transmission electron microscopy ((HAADF-STEM) of a stained membrane present a clear interfacial structure of TFC-PA membrane compared to the non-stained membrane (inset). **c.** Elemental mapping of the PA-PS interface by STEM coupled with energy-dispersive X-ray spectroscopy (STEM–EDS) shows that the PA layer (in magenta) is abundant in nitrogen where PS support (in green) is abundant in sulfur. **d.** Atomic force microscopy (AFM) micrographs for RO and NF membranes show that RO membrane has a higher surface roughness than NF membrane. **e.** 3D visualization of the PA polymer network by HAADF-STEM. The distribution of solid (polymer) density is presented as a heat map (red for high density). The images are adapted with permission from ref. 61 and 63 (a), 66 (b), 67 (c), 54 (d), and 71 (e).

Micrographs from SEM and TEM can also be complemented by surface topographical analysis of AFM images (**Fig. 2d**)[54]. In AFM, the root-mean-square roughness, R_{rms}, defined as

$$R_{rms} = \sqrt{\frac{\sum_{i=1}^{N}(z_i - \bar{z})^2}{N-1}} \tag{1}$$

where z_i is the altitude of pixel i, $\bar{z}$ is the average of z_i throughout the surveyed area, and N is the total number of pixels in the surveyed area. R_{rms} based on AFM topography is often used to facilitate quantitative evaluation and comparison of TFC-PA membrane surface roughness[68,69]. For example, TFC-PA membranes fabricated using MPD are rougher than those fabricated using PIP based on the comparison of their root-mean-square roughness[68]. Because AFM relies on the force interaction between the cantilever tip and the membrane surface, it cannot capture morphological features such as voids and lateral concavities. AFM with line profile analysis has also been used in obtaining the size distribution of surface pores in NF membranes[69]. Recently, 3D tomography based on TEM or STEM has emerged as a powerful imagining technique that can provide valuable information regarding surface morphology and internal pore structure of the PA layer[70–72]. The general idea of 3D tomography is the reconstruction of 3D structure from a series of 2D projection images obtained using different angles. In high-angle annular dark-field (HAADF) mode, STEM-based 3D tomography can also reveal the thickness and density distribution in the polymer film[70,71]. For example, HAADF-STEM can map the nanoscale distribution of polymer density from measured nanoscale intensity distribution (**Fig. 2e**)[71] and yield fractional free volume distribution from which water transport characteristics can be inferred[70–72].

[Au: I suggest adding a H3 heading here of “pore size and structure”]

[H3] Pore size and structure

The internal pore structure of the PA layer can also be probed using non-imaging techniques, most notably positron annihilation spectroscopy (PAS) and X-ray or neutron scattering. Specifically, positron annihilation lifetime spectroscopy (PALS) and Doppler broadening energy spectroscopy (DBES) can be obtained from PAS measurements. In PALS, low-energy positrons are injected into the PA film to form electron-positronium ions that would undergo rapid self-annihilation in polymer rich regions but slow self-annihilation in polymer-deficient regions (pores or free volumes)[73]. The distribution of electron-positronium ion lifetime can thus be translated to the distribution of free volume size. DBES records the momentum densities of γ-ray radiation released during the annihilation from which parameters dependent on the microstructure of the polymer are extracted[74]. DBES has be used to obtain the depth profile of the free volume by varying the positron beam energy in the PA layer[39,74]. One typical way to present the PALS data is to plot the probability density function of the triplet state ortho-positronium (o-Ps) lifetime which also corresponds to free-volume radius (**Fig. 3a**)[39]. The *S* parameter in DBES data as a function of positron incident energy can also be used to reveal depth profile of the free volume in PA layer (**Fig. 3b**)[39].

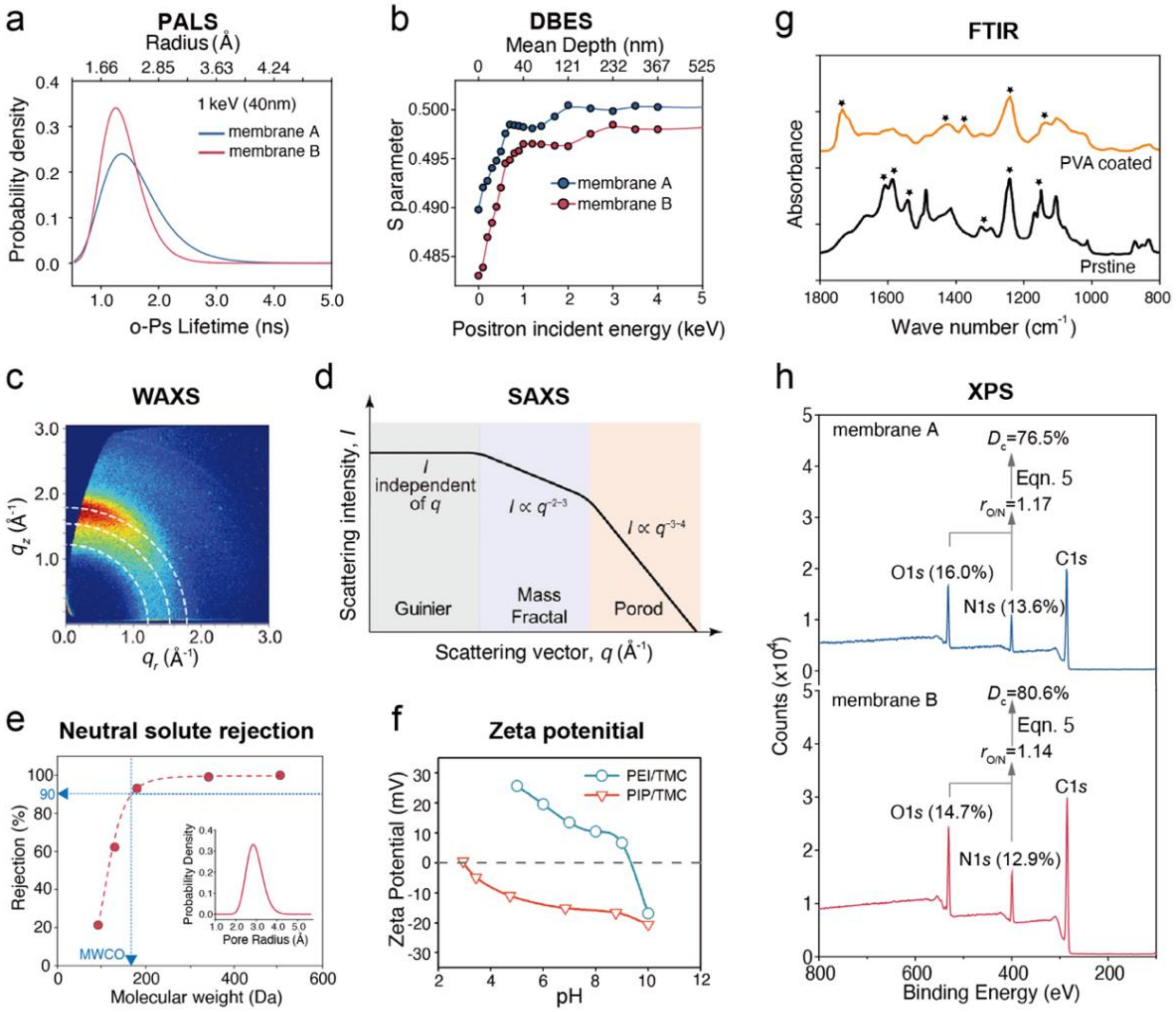

Fig. 3 | **Representative results of non-microscopic characterization of structural, chemical, and interfacial properties of TFC-PA membranes. a.** Pore size distributions of the PA layer derived from of positron annihilation lifetime spectroscopy (PALS). **b.** Evolution of S parameters as a function of film mean depth obtained from Doppler broadening energy spectroscopy (DBES). **c.** Representative pattern from wide-angle X-ray scattering (WAXS) of a PA film. **d.** Representative results from small-angle X-ray scattering (SAXS) of PA bulk dispersion. **e.** Rejections of neutral solutes of different molecular weight. The MWCO corresponds to the molecular weight of the solute rejected by 90%. Inset: pore size distribution of PA active layers fitted log-normal distribution with "sieving assumption". **f.** Zeta potential of the more positively charged TFC-PA membrane made using PEI as the amine vs. that of the more negatively charged TFC-PA membrane made using PIP as the amine. **g.** Comparison of ATR-FTIR spectra between a pristine (uncoated) TFC-PA membrane and a polyvinyl alcohol (PVA) coated TFC-PA membrane. The uncoated TFC-PA membrane shows characteristic peaks (noted with star) of PA bonds and the PS support while the PVA coated membranes reveals additional peaks related to hydroxyl and acetate groups of the PVA coating. **h.** Representative results from XPS measurements and illustration of how it can be used to determine the degree of crosslinking (D_c). The images are adapted with permission from ref. 39 (a, b, e, h), 77 (c), 78 (d), 96 and 104 (f), and 93 (g).

Scattering techniques, such as wide-angle X-ray scattering (WAXS), small-angle X-ray scattering (SAXS), and small-angle neutron scattering (SANS), provide information regarding the polymer structure at different scales depending on the scattering vector q (defined as $q = 4\pi \sin\theta / \lambda$ with θ and λ being the scattering angle and the wavelength of incident radiation, respectively). Specifically, WAXS can provide structural insights at the molecular or atomic scale (0.1-10 Å), whereas SAXS and SANS can unveil mesoscale structural insights (10-1,000 Å).[4,75,76] Representative patterns from WAXS[77] (for polymer film) and SAXS[78] (for bulk polymer) are shown in **Fig. 3c and 3d,** respectively. The data processing and accurate interpretation of results from PALS, WAXS, and SAXS requires expert knowledge from the respective fields and is beyond the scope of this Primer. More detailed explanation of interpreting results from PALS[74,79], DBES[74], WAXS[76], and SAXS[78,80] can be found in the literature.

Although the microscopic, spectroscopic, and scattering techniques discussed above are powerful, some of these instruments are not widely accessible and they do not provide direct information about membrane pore size in the context of solute rejection. One widely practiced method to assess pore size distribution is to measure the rejection of neutral organic solutes of different size (or molecular weight, MW) (**Fig. 3e**). Alcohols[81], sugars[39], poly (ethylene glycols) (PEG)[82,83], poly (ethylene oxide) (PEO)[82] of different molecular weights have been used as the probing solutes. Empirical correlations have been proposed to relate the MW of a solute to its Stokes radius (r_s) using the general form of $r_s = aMW^b$, with a and b being the correlation coefficients that depend on the chemical species[84,85]. The rejections of different organic compounds (concentrations quantified by total organic carbon, TOC) by the sample membranes are measured using filtration experiments and typically plotted against the Stokes radii of the respective compounds. The data points are usually fitted using log-normal distribution as described by the following probability density function (PDF)[56]:

$$\frac{dF(r_p)}{dr_p} = \frac{1}{r_p \ln \sigma_p \sqrt{2\pi}} exp\left[-\frac{\left(\ln r_p - \ln \mu_p\right)^2}{2\left(\ln \sigma_p\right)^2}\right] \qquad (2)$$

where $F(r_p)$ is the cumulative probability of finding pores with radius smaller than r_p, μ_p is the mean pore size, and σ_p is the geometric standard deviation of pore size. Under the assumption that solutes with a Stokes radius smaller than a specific pore size can *all* permeate through the membrane (which we herein refer to as "sieving assumption" for its similarity to sand sieving), $F(r_p)$ is equivalent to the measured rejection of solutes with a Stokes radius equal to or larger than

r_p. Under this framework, μ_p corresponds to the r_s of a solute with a measured rejection of 50% and σ_p correspond to the ratio between r_s of a solute with a rejection of 84.1% and μ_p. In addition, the molecular weight cutoff (MWCO) of a membrane is defined as the molecular weight of a neutral organic solute with a rejection of 90%. Although not as comprehensive as the PDF, MWCO is widely reported as an intuitive parameter quantifying the pore size of commercial membranes and membranes fabricated in laboratory studies.

The inference of pore size distribution from solute size-dependent rejection based on Equation 2 relies on the "sieving assumption" which is reasonable for microfiltration or ultrafiltration where convection is the dominant transport mechanism. In NF and RO where diffusion dominates solute transport, due to steric and hydrodynamic effects, rejection of solutes smaller than pore size is finite (i.e., non-zero) and dependent on solute size[86]. Despite the wide adoption of Equation 2 in many studies of TFC-PA membrane development, the validity of "sieving assumption" is questionable. Alternatively, we can apply the hindered transport model that considers the effects of pore and solute size on partition and transport. Based on the hindered transport model, the intrinsic rejection (or real rejection, to be discussed later when introducing concentration polarization) of a neutral solute is given by[87]

$$R_{int} = 1 - \frac{K_C \Phi}{1 - (1 - K_C \Phi)\exp{(-Pe)}} \tag{3}$$

where Φ is the partition coefficient of the solute, Pe is the Peclet number, and K_C is convection hindrance factor (details for calculating of Pe and K_C can be found in **S1** in **Supporting Information (SI)**). The partition coefficient of a neutral solute smaller than pore size, assuming only steric interactions, is given by[87]:

$$\Phi = \left(1 - \frac{r_s}{r_p}\right)^2 \tag{4}$$

The partition coefficient is zero for solute larger than pore size. The membrane pore size can be estimated using Equations 3 and 4 with solute rejection data obtained using a series of water fluxes.

[H3] Chemical composition

The chemical composition of TFC-PA membranes can be obtained using spectroscopic techniques such as X-ray photoelectron spectroscopy (XPS) and attenuated total reflection Fourier-transform infrared (ATR-FTIR) spectroscopy[88]. XPS provides the elemental composition of a film with a sample depth < 5 nm and is thus ideal for analyzing a PA layer in a TFC-PA membrane without interference from the PS/PES support[89]. In contrast, ATR-FTR provides information about chemical bonds with a sampling depth of hundreds to thousands of nanometers (depending on the incident radiation wavelength), capturing information from the support layer in a TFC-PA membrane[90]. ATR-FTIR and XPS are often used in conjunction to provide information on the composition of a TFC-PA across multiple length-scale[88,90].

Analysis of ATR-FTIR spectra can help identify important functional groups of the PA layer and unreacted monomers (e.g., fingerprint peak assignment of MPD/TMC PA system in **Table S1**) to evaluate the impact of fabrication conditions on the chemical composition of the PA film. Without interference from the microporous polymer support, it can even be employed to quantify the concentration of functional groups (e.g., carboxylic acid groups) to reveal insights of PA film formation[90,91]. ATR-FTIR is also often used to characterize TFC-PA membranes with incorporated additives or surface coatings[90,92,93]. For example, the ATR-FTIR spectrum of uncoated PA layer made from MPD/TMC shows the characteristic peaks of fully aromatic PA at 1608 cm^{-1}(amide I band from C=O stretching), 1540 cm^{-1} (amide II band from N–H bending), and 1590 cm^{-1} (C=C stretching of the aromatic ring)[93], whereas the spectrum of PVA coated membranes reveals all the characteristic peaks related to hydroxyl and acetate groups of the PVA precursor in addition to the peaks from the PA layer (**Fig. 3f**)[93].

XPS, which provides the sample's elemental composition and the relative abundance of each element, plays an important role in TFC-PA membrane characterization because it helps to quantify the degree of crosslinking, an important property of PA layer. To evaluate the degree of crosslinking, the ratio between oxygen (O) and nitrogen (N), or the O/N ratio, is evaluated from the XPS spectrum[88,90]. For PA without additives, the O/N ratio should be 1:1 for a completely crosslinked PA film and 2:1 if the PA is fully linear, i.e., without inter-chain amide bonds (**Fig. S1a in SI**)[94]. Therefore, an O/N ratio closer to 1:1 suggests a higher degree of crosslinking. With the O/N ratio, $r_{O/N}$, the degree of crosslinking (D_c) can be quantified by

$$D_c = \frac{4 - 2r_{O/N}}{1 + r_{O/N}} \tag{5}$$

We note that Equation 5 applies only if the polymer chemistry is purely PA. In cases where the PA layer is modified with additive, D_c may not be assessed using Equation 3 and the O/N ratio may even fall outside the range of 1 and 2. The comparison of the peaks for oxygen (O1s) and nitrogen (N1s) peaks yield the abundance ratio between the two elements ($r_{O/N}$, **Fig. 3g**) from which the degree of crosslinking can be estimated using Equation 5. This XPS-based technique to quantify the degree of crosslinking is valid because probing depth of XPS is only several nanometers which is substantially lower than the thickness of the PA layer.

[H3] **Interfacial properties**

There are two major categories of interfacial properties for TFC-PA membranes: surface charge density/potential and wettability. Surface charge density is important because it dictates Donnan exclusion, which is an important mechanism of salt rejection, and the interaction with charged foulants. A method based on ion adsorption has been developed to quantify the areal density of ionized carboxyl and amine groups from which the areal charge density may be calculated (**Fig. S1b**)[95]. This method is based on the specific adsorption of the probing ions to the target functional groups (e.g., Ag^+ for carboxyl groups and Br^- for amine groups) and the quantification of the probing ion concentration in the eluate using inductively coupled plasma mass spectrometry (ICP-MS)[95,96]. Another method to quantify the carboxyl group density involves the use of uranyl acetate as the probing ion and quantifying the amount of bound uranyl acetate to carboxyl groups using liquid scintillation counting for uranium atoms[97]. In addition, quartz crystal microbalance (QCM) has also been used to determine charge density of TFC-PA membrane via measuring the partitioning of carboxyl group-binding ion (e.g., Cs^+) from the solution into PA layer (**Fig. S1c**)[98,99].

Compared to surface charge density, the zeta potential of the TFC-PA membrane can be measured directly using commercially available streaming potential instrument (**Fig. S1d**)[88,100], and is thus much more widely reported in the literature. Zeta potential and surface charge density are semi-quantitatively related based on double layer theory[101], but the conversion between these two parameters for membranes requires questionable simplifying assumptions. Notably, the zeta potential provides the electrokinetic potential (i.e., the potential at the electrokinetic plane of shear), not the fixed charged density of the membrane, which can lead to erroneous conclusions about the membrane charge characteristics. For example, the measured zeta potential can be negative even for neutrally charged membranes, such as cellulose acetate, likely due to the adsorption of anions to the membrane[102,103]. Hence, quantifying the charge density is more useful than zeta potential for mechanistic studies on the role of membrane charge in salt transport through TFC-PA membranes. Zeta potential, however, can be used for semi-quantitative analyses, such as determining the iso-electric point of the membrane[88,103], or assessing the impacts of surface modification on the electrokinetic properties of the membrane.

The zeta potentials measured using streaming potential technique are reported over a range of pH and can be used to compare the surface charge property of different TFC-PA membranes (**Fig. 4f**)[96,104]. The zeta potential is expected to become more negative at higher pH due to deprotonation of carboxyl and amine groups[96], and is also dependent on ionic strength and possibly the background electrolyte[102], especially when specific adsorption is possible (e.g., with Ca^{2+}). As an example to demonstrate the utility of zeta potential measurements, TFC-PA NF membranes made using polyethyleneimine (PEI) as the amine have been shown to be consistently more positively charged than those fabricated using PIP (commercial NF270) (**Fig. 4h**)[96,104].

The wetting property of a membrane is mostly quantified by measuring water contact angle (WCA) which is relevant in the following aspects. Typically, a PA membrane with more ionized functional groups is more hydrophilic and thus yields a lower WCA[101,105]. Additionally, surface modification is often performed to TFC-PA membranes to improve hydrophilicity, which is believed to be beneficial to water transport and fouling resistance, and WCA is a critical metric to quantify the effect of hydrophilic modification[106–108]. While WCA measurement is relatively simple, its interpretation requires caution for fair comparison. Notably, WCA depends not only on the surface energy of the polymer but also on the surface roughness, following the Wenzel's theory[109]. This caveat is particularly important when comparing WCA between two TFC-PA membranes with dramatically different morphologies.

[H1] Results

[H2] Membrane performance testing

Most membrane performance tests in literature are conducted at the coupon-scale (see **Box 1** for coupon-, module-, and pseudo-module-scale experiments) using either crossflow cells with or without spacer or dead-end stirred cells (typically Amicon®)[110,111]. With a crossflow cell, the feed stream is pressurized using a high-pressure pump and driven through the feed channel filled with a spacer with the feed flow tangent to the membrane. The spacer is important for creating a hydrodynamic condition similar to that in full-scale modules so that a similar degree of concentration polarization (CP) can be achieved at the same crossflow velocity and water flux. The stirring speed in an dead-end cell also needs to be controlled as it also affects the degree of

Box. 1 Coupon-, module- and pseudo-module-scale experiments

For desalination, the primary performance metric of an RO/NF process at the coupon-scale experiment is water flux and salt rejection. Coupon experiments are performed using a small membrane area with a relatively large feed flowrate and with the permeate sent back to the feed tank (except for a small volume sampled for analysis) to maintain a constant feed composition. With coupon experiments, we can assume that the feed channel composition and water flux in the test cell are spatiotemporally constant (assuming no fouling occurs). In contrast to coupon experiments, module-scale experiments are performed with a large membrane area (as in practical desalination plants). Using a module with a large membrane area induces spatial distribution of composition in the feed channel and water flux.

In labs without access to pilot-scale RO/NF systems, we can also perform pseudo-module-scale experiments to extract module-scale information by using a coupon-scale experimental systems without sending the permeate back to the feed tank. Although spatial distribution of feed channel concentration and water flux are absent in pseudo-module experiment, not sending the permeate back to the feed tank induces a temporal variation of water flux and solute concentration in the feed tank that are equivalent to the spatial distributions of the water flux and feed channel concentration in module-scale experiments. The equivalence can be shown if we plot these parameters against water recovery (WR) converted from time (in pseudo-module-scale experiments) and position (in module-scale experiments). In fact, performing pseudo-module experiment is a convenient way to extract equivalent distributions of concentration and flux in a module. Such distributions cannot be obtained readily in module experiments without a distributed sensor network in the module.

In the literature, most membrane performance tests were performed using coupon-scale experiments to understand material performance of membranes at certain feed compositions and applied pressures. Module-scale or pseudo-module-scale experiments are more relevant to elucidating the system-level behavior of membrane modules in practical desalination plants. The simplified experimental setups of the three modes are illustrated in the schematics below.

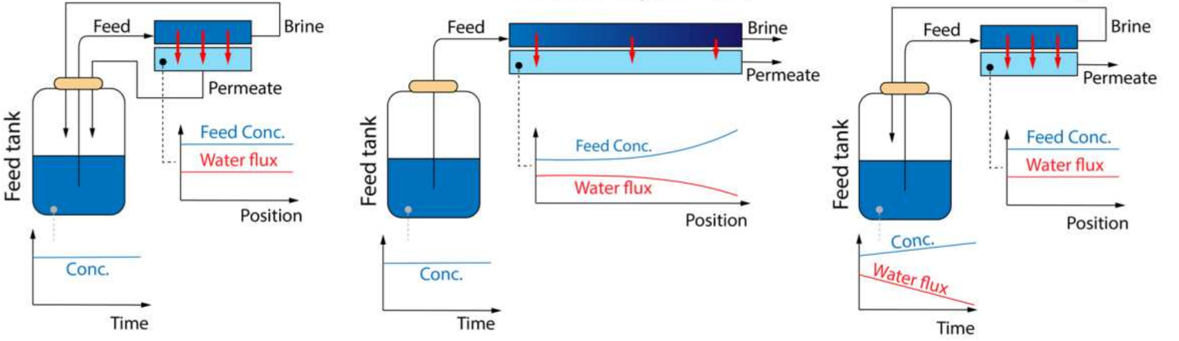

Features	Coupon Exp.	Module Exp.	Pseudo-Module Exp.
Membrane area relative to feed flow rate	small	large	small
Permeate back to feed tank	yes	no	no
Spatial distribution of feed channel concentration and water flux	negligible	yes	negligible
Temporal change of feed tank concentration and water flux	no	no	yes

Before collecting membrane performance data, membranes are pre-compacted by being subject to the operating pressure over a certain duration to minimize the performance artifacts due to membrane compaction[112]. Membrane compaction refers to the compression of the PS/PES support layer and perhaps the PA selective layer of the TFC-PA membrane when operated under high pressure, which is a widely reported, unavoidable phenomenon that affects membrane performance for water permeation and salt retention. For measuring water flux, the membrane is compacted under the testing pressure using deionized (DI) water for several to tens of hours until the flux is stable. For testing salt rejection, the membrane should be equilibrated with the salt solution before collecting the permeate samples. For commercial membranes, the manufacturers often provide pre-conditioning protocols (including pre-compaction and chemical conditioning) that should be followed to attain the manufacturer-specified performance.

[H3] Data collection and preliminary processing.

Water flux can be measured by digital flowmeter or be evaluated based on the temporal evolution of cumulative mass of permeate (m_p) which is typically converted to cumulative permeate volume (V), because volumetric flux (commonly expressed in L m^{-2} h^{-1}, or LMH) is universally reported. For a membrane coupon, the differential (real time) volumetric water flux, J_W, is given by

$$J_W = \frac{1}{S_m}\frac{\mathrm{d}V}{\mathrm{d}t} \tag{6}$$

where S_m is the effective area of the membrane. In coupon-scale experiments without fouling, J_W should be constant. The decline in J_w is due to either fouling, compaction, or increase in salt concentration (and thus osmotic pressure) in the feed solution in pseudo-module-scale experiments. While J_W is often reported in literature for experiments with saline feed solutions, we recommend also measuring J_W with pure water at different pressures to simplify the data interpretation.

Quantifying salt rejection requires measuring the salt concentration in the permeate (with known feed concentration). For desalination, electrical conductivity of the solutions can be conveniently measured and used as a proxy of salt concentration with a calibration curve for dilute solutions. However, if the solutions are highly concentrated or more detailed compositional information on the salt solutions is required, samples can be collected and analyzed for solute concentrations ex situ using techniques proper to the analytes. In general, with the feed concentration (C_F) and permeate concentration (C_P), the observed solute rejection (R_{obs}, also called apparent rejection or measured rejection) is calculated using the following equation:

$$R_{obs} = 1 - \frac{C_P}{C_F} \tag{7}$$

The observed solute rejection, which is to be distinguished from intrinsic rejection (to be discussed), is calculated based on bulk concentrations and is the most widely reported in literature and directly relevant to practical applications. The observed solute rejection is not an intrinsic property of the membrane as it depends on operational conditions, most notably the permeate flux (or applied pressure) employed during the experiments.

[H2] Membrane performance quantification

[H3] Water Permeability

Water flux and salt rejection, experimentally measured to quantify membrane performance, are not intrinsic performance metric of the membrane. For water transport, the intrinsic performance metric is the water permeability coefficient (or permeance) which is typically denoted as A and defined as ratio of pure water flux (as given in Equation 6) and applied pressure (ΔP):

$$A \equiv \frac{J_W}{\Delta P} \tag{8}$$

The most typical unit of A is L m^{-2} h^{-1} bar^{-1} (or LMH/bar). Equation 8 suggests that plotting J_W for pure water vs. ΔP should yield a linear curve with a slope of A. This is generally true for water except in the case when membrane compaction occurs (at high pressure), which again highlights the importance of pre-compacting the membrane to working pressure range for accurate performance evaluation. While the mechanistic interpretation of Equation 8 and A value may differ depending on model framework (i.e., pore flow vs. solution diffusion) chosen to describe water transport in PA membrane, Equation 8 always holds.

In principle, A can also be evaluated from results of PMD experiments with a salt solution, using the following equation:

$$A = \frac{J_w}{\Delta P - \Delta \pi_m} \tag{9}$$

where $\Delta \pi_m$ is the osmotic pressure difference across the PA active layer. For a low-salinity single-salt solution that can be approximated as an ideal solution, $\Delta \pi_m$ can be estimated as

$$\Delta \pi_m \approx \nu RT \Delta C_m \approx nRT\left(C_{F,m} - C_P\right) \tag{10}$$

where n is the van't Hoff factor (i.e., 2 for NaCl), R is the ideal gas constant, T is absolute temperature, $C_{F,m}$ is the salt concentration at the membrane-solution interface on the feed side, and C_P is the salt concentration of the permeate.

Due to concentration polarization **[G]** (CP), $C_{F,m}$ is always higher than the bulk salt concentration of the feed solution, $C_{F,}$ in RO and NF. CP is influenced by the mass transfer coefficient in the boundary layer that depends on the hydrodynamic conditions in the flow channel. Furthermore, the degree of CP is highly dependent on J_w, which renders $\Delta\pi_m$ also dependent on J_w. Although determining A value by filtration of salt solution and equation 9 is theoretically possible, it is more complicated and less reliable than using filtration of pure water and equation 8. We therefore recommend measuring the pure water flux to determine A value.

[H3] Concentration polarization and intrinsic rejection.

Concentration polarization (CP) is an important and universal phenomenon in membrane processes. The occurrence of CP in PMD is caused by the finite kinetics of back diffusion of solutes concentrated near the membrane surface due to convective transport driven by transmembrane water flux[113,114]. With CP, water flux is related to three salt concentrations — C_F, C_P (bulk), and $C_{F,m}$ (interface) — via the CP factor (f_{CP}, also called CP modulus):

$$f_{CP} \equiv \exp\left(\frac{J_W}{k}\right) = \frac{C_{F,m} - C_P}{C_F - C_P} \tag{11}$$

where k is the mass transfer coefficient in the boundary layer (unit: L m^{-2} h^{-1}). For RO membranes with high solute rejection, C_P is negligible compared to C_F and $C_{F,m}$, and Equation 11 can be reduced to $f_{CP} = C_{F,m}/C_F$. Equation 11 is derived based on film theory and k can be estimated using correlations (**Box 2**).

Box. 2 Film model and determination of mass transfer coefficients

In the film model for concentration polarization, a concentration profile of the rejected solutes develops in a hydrodynamically stagnant boundary layer (i.e., the “film”) due to the convective transport of the solutes toward the solute-rejecting membrane and the diffusive transport of the solutes from the membrane surface to the bulk due to concentration gradient[114, 115, 210]. Such a concentration profile is exponential within the boundary layer and renders the interfacial concentration, $C_{F,m}$, to be higher than the bulk concentration, C_F.

Based on film model, $k = D_S/\delta$ where D_S is the diffusion coefficient of the solute in the solution and δ is the thickness of the film layer[114]. The meaning of D_S is relatively clear for neutral solute, more nuanced for a single-salt solution (i.e., binary electrolyte), and intractable for complex solution (e.g., seawater or brackish water). Therefore, the relation $k = D_S/\delta$ is mostly useful for understanding the effect of operational parameters on CP (e.g., to see how hydrodynamics affect δ, and in turn, k). In practical applications, however, k should be evaluated or measured directly. The dependence of k on D_S also suggests that k is dependent on the feed composition.

The boundary layer thickness depends on the hydrodynamic conditions which in turn depends on several factors such as flow channel geometry, flow velocity, and when spacer is used, also the geometry of the spacer. For relatively simple flow channel geometries, correlation equations have been proposed for evaluating the mass transfer coefficient. These equations take the following general form[210,211]:

$$Sh \equiv \frac{kd_h}{D_S} = aRe^b Sc^c$$

where Sh is the Sherwood number, Re is the Reynold number ($Re \equiv ud_h/\nu$, with u and ν being the flow velocity and kinematic viscosity, respectively, and d_h is the hydraulic diameter for the channel), Sc is the Schmidt number ($Sc \equiv \nu/D_S$), a, b and c are the correlation coefficients depending on flow conditions. Correlations for typical channel geometries are summarized in **Table S1**.

The correlation method is less reliable or useful when the feed channel contains a spacer, especially when the spacer can have different mesh geometries. An alternative way to evaluate k is based on a combination of Equations 9-11[212]:

$$\frac{J_W}{k} = \ln\left[\frac{\Delta P - J_W/A}{nRT(C_F - C_P)}\right]$$

Experimentally, we can use a single-salt feed solution with a concentration C_F, increase ΔP and measure J_W and C_P (C_P may be dropped for RO membranes). We then can plot the right-hand-side of the above Equation vs. J_W and find the slope which equals $1/k$. This method allows experimental determination of k.

Because CP renders $C_{F,m} > C_F$, the observed solute rejection evaluated using Equation 5 is an underestimation of the intrinsic (or real) rejection defined as

$$R_{int} = 1 - \frac{C_P}{C_{F,m}} \tag{12}$$

When k is known, the intrinsic rejection, R_{int}, and the observed rejection, R_{obs}, can be interconverted using the following relation[49]:

$$R_{int} = \frac{f_{CP} R_{obs}}{1 - R_{obs} + f_{CP} R_{obs}} \tag{13}$$

[H2] Models and performance metrics for salt transport

While R_{int} reflects inherent characteristics of the membrane to a greater extent than R_{obs}, it is still not an intrinsic parameter of the membrane (for a given salt species). In this section, we present several models to extract more intrinsic membrane parameter for salt transport from experimental measurements.

[H3] Solution-diffusion model

The most widely used model for mass transport is the solution-diffusion (SD) model, which assumes that water and solute species transport independently via first dissolving (or partitioning) into the PA layer, then diffusing across the layer under respective concentration gradients, and finally partitioning out of the layer into the permeate (**Fig. 4a**)[19,20]. The SD model is convenient because it enables a description of the transport characteristics of a TFC-PA membrane using two parameters: the water permeability coefficient as defined in Equation 8 (or 9) and the solute permeability coefficient, B (unit: LMH), defined as

$$B \equiv \frac{J_S}{\Delta C_m} = \frac{J_S}{C_{F,m} - C_P} \tag{14}$$

where ΔC_m is the solute concentration difference across the PA active layer, considering CP that brings C_F in the bulk to $C_{F,m}$ at the membrane surface. Both Equations 8 (or 9) and 14 are based on the principle that, for each species, the flux equals the product of the respective driving force and the permeability coefficient. With further derivations (**S2**), it has been shown that the B value can be calculated using J_W, R_{obs}, and k using the following equation[49]:

$$B = \frac{\frac{J_W}{R_{obs}} - J_W}{f_{CP}} \tag{15}$$

Since J_W and R_{obs} can be directly measured and there is an independent way of evaluating k using Equation 11, B can be experimentally determined.

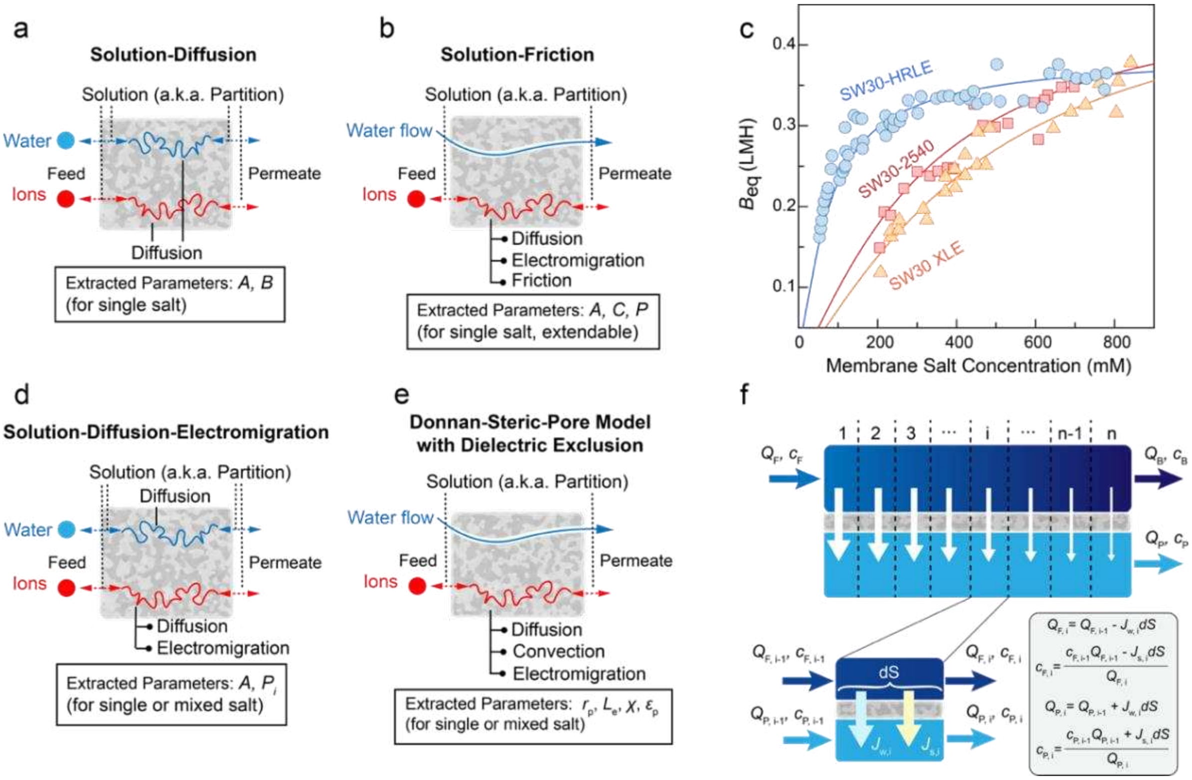

Fig. 4 | **RO/NF models at the coupon and module scale. a.** Solution-diffusion (SD) model with water permeability coefficient (A) and solute permeability coefficient (B) as the extracted parameters. **b.** Solution-friction (SF) model with A, transport factor (P), and charge factor (C) as the extracted parameters. **c.** Dependence of equivalent salt permeability coefficients (B_{eq}) on feed concentration (C_F) for different RO membranes base on SF model (adapted from ref. 118 with permission). **d.** Solution-diffusion electro-migration (SDEM) model which considers electromigration in addition to diffusion. The extracted parameters are A and ion permeabilities, P_i. One permeability will be extracted for each ion. The SDEM model has been commonly used for modeling ion transport in NF with mixed salt feed solution. **e.** Donnan Steric Pore Model with Dielectric Exclusion (DSPM-DE). The four major parameters to be extracted from the DSPM-DE is pore size (r_p), effective thickness (L_e), effective charge density (X) and dielectric constant within the pore (ε_p). These parameters can be extracted by either a multi-step experimental procedure[76] or the global optimization technique[127]. **f.** Illustration of module-scale model based on finite difference. The equations in the box describe the mass balance of water and solutes (ions) between adjacent cells, considering local water and solute fluxes. Local water flux ($J_{w,i}$) and solute flux ($J_{s,i}$) are determined based on local solution composition and operating conditions using a selected coupon-scale model (chosen from SD, SF, SDEM, DSPM-DE, or others).

With this framework based on SD model, the separation performance of each TFC-PA membrane is summarized as a pair of value, A and B, evaluated using Equations 8 (or 9) and 15, respectively. The ratio A/B is also widely reported in literature to quantify the water/solute selectivity[49,115] (See Section S3 where we discuss why the widely claimed "intrinsic perm-selectivity tradeoff" may not be necessarily intrinsic). A large A/B ratio represents a membrane that favors water permeation but not solute permeation, which facilitates high solute rejection. In fact, R_{obs} has been expressed as a function of A/B using the following equation[49]:

$$R_{obs} = \frac{\frac{A}{B}(\Delta P - f_{CP}\Delta\pi)}{\frac{A}{B}(\Delta P - f_{CP}\Delta\pi) + f_{CP}} \tag{16}$$

where $\Delta\pi$ is the bulk osmotic pressure difference that equals $nRT(C_F - C_P)$ for an ideal solution. Equation 16 reveals that a large A/B ratio and a small f_{CP} are both beneficial to achieving a higher observed solute rejection. The values of A and B are reported in an Open Membrane Database (OMD) which is a web-based database with calculation and analysis tools[116]. It is, however, important to recognize that most studies (>95%) did not report k or f_{CP}, and a k value of 100 LMH was arbitrarily assumed in OMD for calculating the A and B values for membranes from those studies. The OMD team also proposed a set of standard testing conditions for SWRO and BWRO (**Table S3**)[116]. Regardless of the mechanistic correctness (which belongs to another discussion beyond the scope of this paper), the SD framework for characterizing membrane performance has at least two major limitations. First, it is widely recognized that the B coefficient, even for a given salt, is not a constant but rather depends on the salt concentration near the membrane surface (i.e., after considering the CP)[25,117], which makes the comparison of B values between different TFC-PA membranes only meaningful at the same interfacial salt concentration. For PMD operations, both feed salt concentration and permeate water flux vary over a wide range, casting doubts on the comparison of B between different experiments[25]. Second, the SD framework cannot explain negative rejection (i.e., $C_P > C_F$) commonly observed in many NF experiments with mixed electrolytes.

[H3] Solution-friction model

The solution-friction (SF) describes the coupled transport of water and salt in RO membranes. The model combines ion partitioning between the solution and membrane phase (like that in the SD model) and microscopic description of ion transport within the PA layer considering the interactions between the species (i.e., salt ions, water molecules, and the membrane) (**Fig. 4b**)[25,118]. The SF model is derived based on force balances for water and salt ions transport through the membrane. Specifically, the frictional force acting on the salt ions is balanced by the driving force, i.e., the gradient of chemical potential of salt ions. Similarly, as water transport through the membrane, the hydrostatic pressure is balanced by the friction between water molecules and the membrane as well as water molecules and salt ions[119].

Based on the SF model, Biesheuvel, Elimelech, and colleagues proposed a new framework to characterize PMD membranes to extract concentration-independent parameters to quantify membrane performance[118]. Under this new framework, the observed rejection is given by

$$R_{obs} = 1 - \frac{P}{J_W}\left(\sqrt{\left(\frac{C}{C_F}\right)^2 + \exp\left(\frac{2J_W}{k}\right)} - \frac{C}{C_F}\right) \tag{17}$$

where P is called the transport factor that quantifies the "conductance" of the membrane to salt transport considering partitioning, diffusion, and frictions; and C is called the charge factor integrating charge density and non-Donnan partition coefficient[120]. Detailed derivation of Equation 17 and definitions of P and C can be found in the work by Biesheuvel et. al[118,120].

Recognizing that B is not an intrinsic parameter, the concentration-dependent *equivalent* salt permeability coefficients, B_{eq} (defined based on Equation 14), can still be evaluated under the SF framework:

$$B_{eq} = P\left(\sqrt{\left(\frac{C}{C_{F,m}}\right)^2 + 1} - \frac{C}{C_{F,m}}\right) \tag{18}$$

We use "equivalent" instead of "observed" (as in the original manuscript) to reserve "observed" for values that are measured or evaluated without considering CP (whereas Equation 18 already considers CP). Equation 18 shows the dependence of B_{eq} on C_F, which is summarized in **Fig. 4c** for several commercial membranes[118]. In general, B_{eq} increases with increasing interfacial feed concentration, $C_{F,m}$, and approaches a limit at high $C_{F,m}$, which suppresses Donnan exclusion. The dependence of B_{obs} on interfacial concentration was found to be stronger for some membranes (e.g., SW30 series) and almost absent for other membranes (e.g., XLE)[118].

With this SF-based framework, we can vary J_W by changing the applied pressure at a given C_F to measure R_{obs}, and fit the data of (J_W, R_{obs}) using Equation 17 to extract P and C, assuming that k can be independently determined using a correlation or an experimental method based on Equation 11. Both Equations 17 and 18 reveal that a lower P and a larger C are beneficial to solute rejection (i.e., a higher R_{obs} and a lower B_{eq}).

Comparing the SD framework[20] and this new SF-based framework by Biesheuvel et. al.[25,118], the SD framework quantifies the membrane performance (for removing a specific salt) using two parameters, A and B; whereas the SF-based framework quantifies the membrane performance using three parameters, A, P and C. For modeling module-scale behavior where feed concentration varies spatially along the feed channel, the SF-based framework based on Equation 17 provides an elegant model to account for concentration dependence and is thus superior to the SD framework. For comparing performance of different membranes under similar operating conditions, however, because of the difficulty of visualizing (A, P, C) data with clarity and giving simple interpretations of P and C to non-experts in membrane transport theory, the SD framework based on (A, B) may still be preferred, despite its lack of rigor and mechanistic insights. An additional practical advantage of the SD framework is that evaluation of B in principle only requires one measurement (based on Equation 15, assuming k has been determined), whereas the determination of P and C requires fitting Equation 17 using multiple data points collected from a series of experiments.

[H3] Other models and global parameter determination

Other models have been used, mostly in NF (but in principle extendable to RO), for fundamental understanding, modeling module-scale behavior, and occasionally for comparing membrane performance. One example is the solution-diffusion electro-migration (SDEM) model, which keeps the diffusion and electro-migration terms in the extended Nernst-Planck equation but drops the convection term (**Fig. 4d**)[121]. SDEM model still uses the concept of permeability, but the permeability is defined for an ion species instead as for a salt species as in the SD model. With permeability for ions and the inclusion of the electro-migration term, the SDEM model allows the prediction of negative rejection of ions in NF with mixed salt feed solutions[121,122], which is impossible with the simplistic SD model. Sharing the same weakness of the SD model, however, the SDEM model provides no mechanistic description of the dependence of the ion permeability on feed composition. An imperfect but practical solution to address this challenge is to develop empirical correlations between ion permeabilities and (interfacial) feed composition from experimental data[123].

Another widely used model is the pore flow model, or the so called Donnan Steric Pore Model with Dielectric Exclusion (DSPM-DE)[87,124]. The DSPM-DE considers water and ion transport through tortuous cylindrical pores with charge and accounts for steric, Donnan, and dielectric exclusions and hindered transport of solutes within pores (**Fig. 4e**)[124]. Although the DSPM-DE has many simplified assumptions and mechanisms that might be questionable (e.g., the inclusion of dielectric exclusion), it can provide some mechanistic insights of how the change in certain membrane properties (e.g., pore size, charge density) would affect membrane separation performance in a way that the other more phenomenological models cannot provide (e.g., pore size is not a parameter in the SD, SDEM, or SF model). A detailed review of the DSPM-DE with a step-by-step instruction of how to extract parameters for the model was provided by Wang and Lin[86]. The DSPM-DE has been used for modeling module-scale behavior for desalination and selective solute separation.

For all these models discussed above, from the simplest SD model to the more complicated DSPM-DE, methodologies have been developed to extract each parameter in the model via multi-step procedures. Depending on the model complexity and structure, stepwise (or sequential) determination of model parameters typically involves different types of experiments and may face intrinsic challenges in uncertainty propagation[86]. Alternatively, a global optimization approach can be used for parameter determination[125,126]. Briefly, a series of data (water flux and salt rejection) is collected under different combinations of feed concentration and applied pressure. With a chosen model framework, a set of model parameters that best fit the collected data series can be found using non-linear regression.

Module-scale modeling and system performance evaluation

With an experimentally validated coupon-scale model, we can model the module-scale mass transfer for PMD[127]. While real PMD modules are typically of spiral-wound configuration with a relatively complex flow pattern, a simplified 2D model based on finite difference method is sufficient for most applications[128,129]. The 2D model considers both the mass transfer normal to the membrane (i.e., local water and solute fluxes) and the mass balance in the crossflow direction (**Fig. 4f,** details in module-scale modeling can be found in Section **S4**).

The solution to the model contains distribution of local water and solute fluxes, flowrates and concentrations in the feed and permeate streams, among other parameters. From the model solution we can evaluate, in addition to WR, important module-scale performance parameters such as average water flux, $\overline{J_W}$, and module-scale solute rejection, R_{mod}:

$$\overline{J_W} = \frac{Q_P(WR)}{S_m} \tag{19}$$

$$R_{mod} = 1 - \frac{C_P(WR)}{C_{F,0}} \tag{20}$$

With the solution to the module-scale model, the specific energy consumption (SEC, i.e., energy consumed per volume of permeate) of the desalination processes can also be evaluated. Besides parameters used in module-scale modeling, SEC is also dependent on system configuration (e.g., multi-stage, multi-pass, closed-circuit) and the efficiencies of pumps and energy recovery devices (ERDs)[130]. Analyses of SEC with different configurations and levels of complexity are available in literature[131,132].

[H1] Applications

[H2] Seawater desalination

RO is the dominant technology for seawater desalination with a global capacity of ~ 36 million m^3 day^{-1} [133–135]. A single-pass SWRO treatment train consists of seawater intake, pre-treatment, RO unit process, post-treatment, and brine discharge (**Fig. 5a**). A typical SWRO system treats water with salinities ranging from 30 to 45 g L^{-1}, and operates at around 50% WR to minimize energy consumption and fouling[134] . Two-pass RO is typically employed to further enhance permeate water quality and reduce the concentrations of certain species, such as boron and chloride [136–138] (**Fig. 5b**). The working pressure of SWRO ranges from 50 to 80 bar[139] and the typical average water flux is controlled to below 20 LMH for both fouling prevention and energy consumption considerations[140,141]. The SEC of the entire treatment train, including intake, pre-treatment, and post-treatment, ranges from 2.5 to 4.0 kWh m^{-3} for modern SWRO plants[141,142] and is below 2.8 kWh m^{-3} for the state-of-the-art facilities[136,142]. Typically, 60% or more of the total SEC is contributed by the RO unit process[136]. The relatively low SEC can is achieved partially due to the implementation of energy recovery devices that can recover up more than 95% of the energy embedded in the pressurized brine (retentate) stream[136].

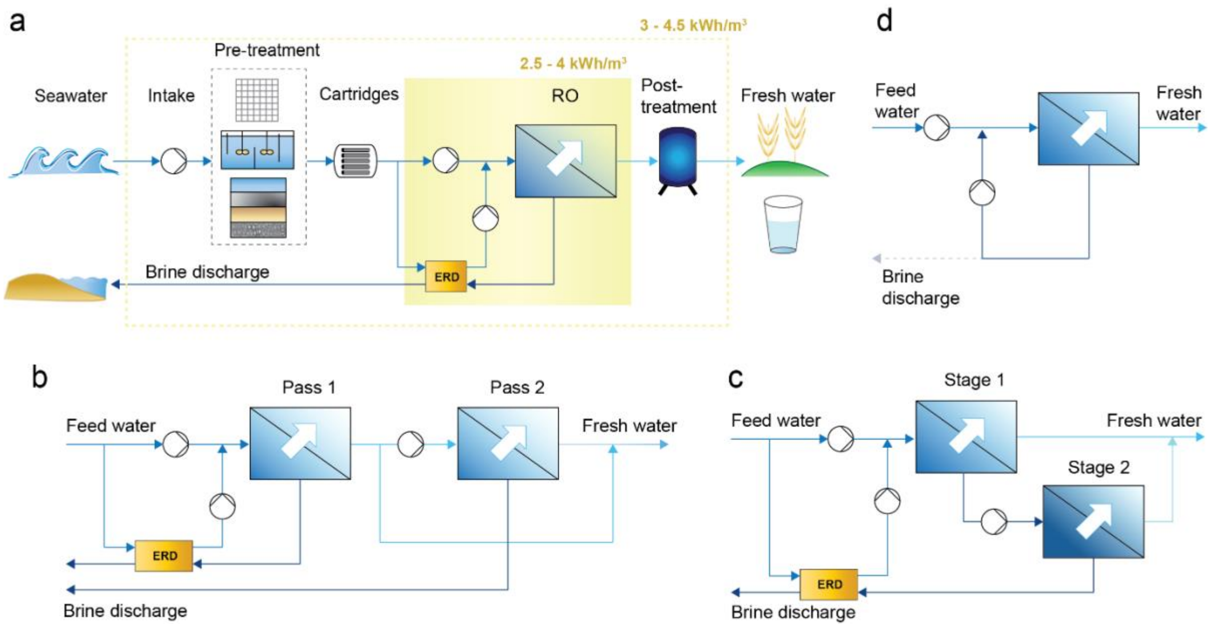

Fig. 5 | **RO treatment train and configurations. a.** Illustration of an SWRO desalination plant showing the various unit processes including intake, pre-treatment, RO, post-treatment, and brine discharge. **b.** Two-pass RO operation where the permeate of the first pass is sent to the second pass as feed solution to further improve the permeate quality. **c.** Two-stage RO operation where the retentate from the first stage (lower operating pressure) is further pressurized and sent to the second stage (higher operating pressure). The permeate from both stages are collected as the product water. **d.** Closed-circuit RO (semi-batch RO) operation where the retentate is recirculated and mixed with the feed solution before entering RO module again. The operating pressure is increased over time to overcome the increasing osmotic pressure due to accumulation of salt in the closed-circuit. ERD, energy recovery device.

The levelized cost of water (LCOW) varies widely due to numerous factors, including local prices of electricity and indirect capital expenses. Economy of scale effects have played a major role in recent years in driving down the costs of desalinated water. For example, the plant at Al Taweelah, United Arab Emirates, produces water at $0.49\ \$\ m^{-3}$ with an installed capacity of 331.8 million m^3 per year[135], while the soon operational Sorek II plant in Israel is expected to produce 200 million m^3 per year at $0.41\ \$\ m^{-3}$ [143].

[H2] Brackish water desalination

Brackish water refers to water with a salinity or total dissolved solids (TDS) beyond 0.5 g L^{-1} (typically below 10 g L^{-1})[144] and is usually groundwater and wastewater but can also be surface water with elevated TDS. Brackish water desalination is critical to augmenting freshwater supply in dry inland regions, comprising over 21% of the total worldwide desalination capacity[145]. Brackish water desalination has been practiced at large scales for decades in many countries, such as Israel, Spain, Tunisia, the US, and the UK[144,146,147]. In the US, RO dominates brackish water desalination applications, accounting for more than 85% of the installed systems to date[148].

Typical operating pressure for BWRO ranges from 5 to 30 bar, with a WR of 75−85%[149]. Though BWRO has a higher WR and a lower brine ratio compared to SWRO, brine management remains a major challenge in inland BWRO. BWRO usually uses multiple stages (two stages illustrated in **Fig. 5c**) to improve WR and reduce energy consumption[149,150]. More recently, a new system configuration called closed-circuit RO (CCRO) has been developed. In CCRO, the retentate is recirculated in the closed-circuit and blended with the feed water before entering the RO module as the feed solution (**Fig. 5d**). As salt concentration and osmotic pressure in the closed-circuit increase over time, the applied pressure is ramped up accordingly. CCRO has the benefit of reducing SEC compared to single-stage RO and possibly reduced capital cost compared to multi-stage RO. CCRO has also been shown to be capable of reducing fouling/scaling due to flow circulation and its ability to maintain a relatively low water flux everywhere in the module at all time.

SEC of BWRO processes is approximately 0.8-2.5 kWh m^{-3}, depending on the feed salinity, permeate quality requirement, and WR[146,151,152]. Compared to SWRO, BWRO typically operates at a lower pressure and recovers more water which results in smaller brine volumes. Installing an ERD is thus not always beneficial because the energy saving may be eclipsed by the additional capital and maintenance costs[144,153]. The LCOW for BWRO is typically lower than that of SWRO (at the same scale) but highly dependent on scale and site-specific conditions[144].

[H2] Water Reuse

Water reuse has grown dramatically in the past decades[154]. End uses for municipal wastewater reuse projects can be classified into non-potable and potable[155], and range from agricultural and industrial to domestic consumption, with domestic consumption experiencing considerable growth over the past few years[154]. Depending on the application, requirements on the product water vary, resulting in different process configurations and levels of treatment. Multiple barrier treatment trains are characteristic of potable reuse systems to guarantee maximum safety of the product water[156]. Typical barriers consist of full advanced water treatment, comprising filtration and advanced oxidation, blending with natural waters, and efficient source control programs[156,157]. Membrane based approaches have gained predominance in potable reuse applications[158], and this trend is likely to continue, prompted by the increasing implementation of multiple barrier systems[154].

Potable reuse systems are categorized into direct (DPR) and indirect (IPR), depending on whether the produced water is sent through an environmental buffer before entering drinking water plant[159]. In these processes, feed TDS is typically around 1 g L^{-1} and up to 85% of water is recovered[158]. Owing to the low feed TDS, typical operating pressures do not exceed 15 bar[155]. Energy consumption for potable reuse systems is generally between 1 and 2 kWh m^{-3} [159], although slightly wider ranges have been reported[160], with the variability attributed to process configurations, economies of scale aspects, and if the system is for DPR or IPR. Due to the lower feed osmotic pressure and thus higher attainable WR, water reuse processes are typically configured in multi-stage trains with inter-stage pumping to minimize energy consumption[158,159]. Like BWRO, incorporation of ERD is not necessarily favorable in economics (as in SWRO) and must be evaluated wholistically. The LCOW for water reuse varies with location, technology, and plant capacity but is generally lower than that for SWRO at the same scale[155].

[H2] Brine concentration or brine volume reduction

Hypersaline wastewater treatment is an important frontier where pressure-driven membrane processes can be disruptive[161]. Due to its superb energy efficiency, conventional RO has already been incorporated in most treatment trains for zero liquid discharge (ZLD) and minimal liquid discharge (MLD), typically concentrating the brine to a TDS of 70 g L^{-1} (**Fig. 6a**)[145,146]. Beyond this TDS, a thermal evaporative process, most commonly mechanical vapor compression (MVC), is used to further concentrate brine or even achieve crystallization[162]. However, MVC as well as other thermal technologies are energy intensive, lack modularity, and have a high capital cost due to the use of expensive corrosion-resistant alloys. Recent analysis has shown that replacing MVC with pressure-driven membrane processes for concentrating brine at the very high TDS range (70~250 g L^{-1}) has the potential to dramatically reduce the cost of MLD or ZLD[162]. There are two main strategies to enable pressure-driven membrane process to concentrate hypersaline brine: (1) developing membranes and modules for high-pressure RO (HPRO) with much higher working pressure (> 100 bar)[163,164] and (2) developing RO variants that can handle hypersaline brines with an osmotic pressure that is much higher than the applied pressure[165–167].

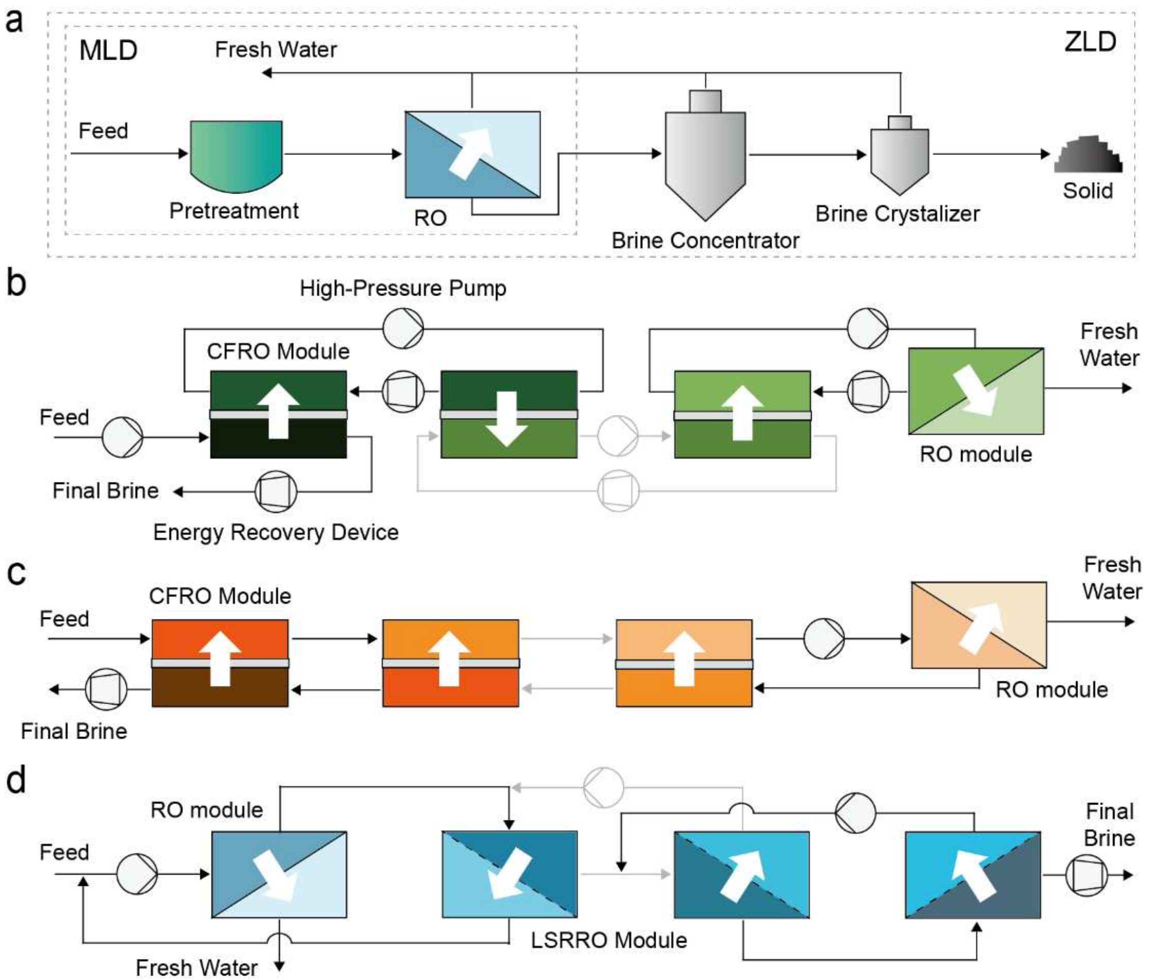

Fig. 6 | **The use of RO and its variants in brine management. a.** A representative treatment train for minimal liquid discharge (MLD) and zero liquid discharge (ZLD) where the brine is, after pre-treatment, concentrated by conventional RO to a relatively high TDS and then treated by an MVC-based brine concentrator and/or brine crystallizer. **b.** Osmotically assisted RO (OARO). **c.** Cascading osmotically mediated reverse osmosis (COMRO). Both OARO and COMRO utilize counter-flow RO (CFRO) modules with moderate TDS water in the permeate channel to render the trans-membrane osmotic pressure difference lower than the osmotic pressure of the solution in the feed channel. **d.** Low-salt-rejection RO (LSRRO) where salt-leaking NF membranes are used to render the trans-membrane osmotic pressure difference lower than the osmotic pressure of the solution in the feed channel. LSRRO modules resemble conventional RO modules in design and do not require a counter-flow configuration. All the RO variants, including OARO, COMRO, and LSRRO, will adopt multi-stage with one conventional RO stage to achieve a high water recovery.

Except for the elevated operating pressure, the working principle of HPRO is the same as that of conventional RO. In theory, raising the operating pressure to 300 bar can enable HPRO to concentrate brine to a TDS over 250 g L^{-1} with an estimated energy consumption an order of magnitude lower than that of MVC[163]. However, existing RO membranes and modules are not designed to work in this ultrahigh pressure range and will suffer from problems such as membrane compaction, bulging of membranes into spacer opening, and module failure[112]. Thus, designing membranes and modules that can sustain high operating pressure is key to advance HPRO.

To handle high TDS brine without very high operating pressure, variants of RO with counter-current flow modules, such as osmotically assisted RO[166] (OARO, **Fig. 6b**) and cascading osmotically mediated reverse osmosis[165] (COMRO, **Fig. 6c**), are being actively developed. Unlike conventional RO, these RO variants use counter-current flow modules and introduce a saline stream with a moderate TDS in the permeate channel to reduce the osmotic pressure difference across the RO membrane. Water permeation from the high TDS feed stream to the moderate TDS permeate stream occurs because the applied pressure, although lower than the feed osmotic pressure, exceeds the transmembrane osmotic pressure difference. For OARO with three stages, the brine can be concentrated to a TDS beyond 200 g L^{-1} with an energy consumption substantially lower than MVC[168,169].

Recently, another RO variant called low-salt-rejection RO (LSRRO) was developed using conventional spiral-wound modules but with low-salt-rejection membranes (**Fig. 6d**)[167]. The “leakage” of salt in LSRRO reduces the transmembrane osmotic pressure difference and enables concentrating a high TDS feed stream using an operating pressure lower than the feed osmotic pressure. Theoretical analysis showed that a 3-stage LSRRO process can concentrate the brine to a TDS beyond 200 g L^{-1} with an energy efficiency potentially even higher than that of OARO[169]. LSSRO is also more practical than counter-current flow RO variants because LSSRO can use existing spiral-wound module design and does not have the challenge of internal concentration polarization[167]. Therefore, LSRRO is a highly promising technology for brine concentration.

[H1] Reproducibility and data deposition

The main challenges of reproducibility are in membrane fabrication and performance evaluation. Common to many areas of material synthesis research, results from some studies on TFC-PA membrane fabrication have been anecdotally reported to be poorly reproducible. Notably, IP is a complex process with many influencing factors and our understanding of the IP process is still far from thorough. While many researchers try to report, with goodwill, as many experimental details as they consider important, they may still miss to report subtle parameters that turn out to be pertinent in ways that most people are not aware of.

For instance, the wetting state of the PS/PES support by the aqueous amine solution is believed to have strong impacts on the morphology and performance of a TFC-PA membrane[170]. In addition to additive species and concentration, which are relatively easy to control, the wetting state is also influenced by other factors such as temperature, humidity, removal of excess aqueous solution using blotting or rolling, and when and how to initiate the IP process after the support is wetted. Some of these factors are difficult to quantify, and none of these factors is commonly reported in the literature. Other information that may be critically important but rarely reported includes when and how to terminate the IP process, as well as how to perform post-treatment (annealing) and store the fabricated membrane samples. Better controlling these factors may significantly enhance the replicability of the properties and performance of TFC-PA membranes fabricated in academic labs. But it would require accurate quantification and comprehensive reporting in publications, which is both non-existing and expectedly challenging.

Another key challenge for reproducing results from the same commercial membranes, or more commonly, fairly comparing the performance between different lab-fabricated membranes, stems from the inconsistency in performance testing method which has been discussed in detail in **Section 3**. It is important to recognize that measured salt rejection (R_{obs}) is not an intrinsic performance parameter of a membrane but depends on water flux, salt concentration, and the degree of CP. A better understanding of the basic transport theory in PMD as summarized in this Primer will help "membrane material scientists" to conduct more meaningful performance testing and report data that is relevant and useful for cross-experiment comparison.

Additionally, the solution pH and temperature can also have substantial influence on the performance of PMD membranes[171,172]. Their impacts are known but have not received sufficient attention from the broader membrane community. The solution pH influences the ionization of functional groups in PA layer and thus the membrane charge, which in turn affects the salt flux through the TFC-PA membrane[172]. In addition, the feed temperature has been shown to have significant impact on water permeability mainly via its impact on liquid viscosity, which renders water and solute fluxes sensitive to temperature[171]. Therefore, we recommend documentation of solution pH and temperature in the data deposition. For commercial membranes, temperature corrections factors to account for the impact of temperature on water flux are often provided by the membrane manufacturers and water fluxes measured at different temperatures can be converted to flux value at a standardized temperature of 25 °C[173,174].

The open membrane database (OMD) provides an excellent platform to improve data reproducibility and comparability by recommending best practices and standardized experimental conditions for data acquisition[116]. The OMD is also the ideal repository for data deposition with its standardized entry forms. The data analysis tools ("calculators" on the OMD website) are also highly instrumental to membrane material scientists who are not well familiar with the transport theory.

[H1] Limitations and optimizations

[H2] Susceptibility to chlorine oxidation

In modern desalination plants, chlorine is added to feedwater in the pretreatment stage to prevent membrane biofouling[175,176]. However, aromatic PA membranes suffer from oxidative damage due to the susceptibility of the amide links to chlorine[11,177,178]. The lack of chlorine resistance requires a de-chlorination step before water entering the RO modules to protect the PA membrane from biofouling, followed by a re-chlorination step to control microorganisms in the distribution system[175]. Developing membrane with higher chlorine tolerance and similar desalination performance to existing TFC-PA RO membranes is a strategic priority as it would eliminate the need for de-chlorination and re-chlorination, and thus simplify the process scheme, reduce chemical dosage, improve process reliability, and reduce the overall levelized cost[179].

Several approaches have been explored to fabricate chlorine-resistant RO membranes[11]. The first and the most promising approach is to use alternative chemistry to fabricate polyester, sulfone, and epoxide-based membranes that are less susceptible to chlorine attack[15,37,180,181]. However, the separation performance (i.e., water flux and salt rejection) and long-term stability of these membranes based on alternative chemistries still need to be improved to match that of TFC-PA membranes. The second approach is to apply on the TFC-PA membrane a protective coating such as polyvinyl alcohol (PVA) and poly (N,N-dimethylaminoethyl methacrylate) (PDMAEMA), which often compromises water flux[182–185]. The third approach turns to nonpolymeric materials such as carbon molecular sieves, graphene, and graphene oxide, but poor scalability of these materials hinders mass manufacture and practical applications[186–188]. It is important to note that these emerging membranes exhibit poor salt rejection compared to TFC-PA membranes even for very small area membrane coupons[15,37,182,184,187].

[H2] Insufficient removal of small neutral solutes

Compared to salt rejection, RO's performance in rejecting small neutral solutes of concern is insufficient in some scenarios. The first problematic small neutral solute is boron, which is dominantly present as neutral boric acid at seawater pH. Seawater contains 5-7 mg L^{-1} boron. While the updated WHO guideline for boron concentration in drinking water is 2.4 mg L^{-1} [189] (it used to 0.5 mg L^{-1} before 2009), the recommended boron level for irrigation water is 0.3-0.5 mg L^{-1} [190], requiring 90-95% rejection of boron (vs. 80-93% for most commercial SWRO membranes[191,192]). Two-pass RO has been adopted to further remove boron, where a low-pressure, high-flux RO is employed to further polish the 1st pass SWRO permeate, adding capital cost to the desalination process[191,193]. The second category of small neutral solutes of concern are disinfection byproducts (DBPs)[194], with a famous example being N-nitrosodimethylamine (NDMA)[195]. The rejection of small and neutral DBPs by RO membranes varies over a wide range depending on the solution chemistry and operating conditions but is often insufficient for portable reuse[10]. Thus, extra pre- or post- treatments are required to further remove small and neutral DBPs until RO membranes with better performance are available.

[H2] Membrane fouling

Like other membrane processes, PMD faces the challenge of membrane fouling. Membrane fouling refers to the deposition of undesirable substances on the membrane surface, which compromises water permeation and permeate quality[196]. Based on the foulant type, fouling on PMD membranes can be classified into biofouling, organic fouling, inorganic fouling (or mineral scaling), and colloidal fouling[197]. Biofouling is a complex process involving microorganism adhesion and biofilm formation on membrane surfaces[198]. The biofilm consists of bacteria and extracellular polymeric substances (EPS) with diverse compositions and is dependent on the environment and bacterial community[199–201]. Organic fouling is caused by natural and effluent organic matter such as humic substances and proteins[202,203]. Mineral scaling occurs when sparsely soluble salts precipitate out of the solution and subsequently deposit and grow on the membrane surface. Depending on the source of water, typical scalants include gypsum ($CaSO_4$), calcite ($CaCO_3$), and silica (SiO_2)[176]. Colloidal fouling is caused primarily by the deposition of naturally colloidal particles which are primarily minerals[204]. The primary indicator of fouling in most bench-scale experiments performed at constant pressure is flux decline[204]. However, real desalination plants are typically operated at constant water flux, and the practical indicator of fouling is thus increase in applied pressure.

Extensive research has been performed to better understand and mitigate the various types of membrane fouling in PMD and other membrane processes. Effective fouling mitigation strategies include pretreatment, membrane cleaning, and membrane surface modification[197,205]. Typical pretreatment processes include coagulation/flocculation followed by media or membrane filtration to mitigate colloidal, organic, and biofouling, chlorination to reduce biofouling, and softening or adding antiscalant to inhibit mineral scale formation[176,206]. These pretreatment processes can slow down, but not eliminate, fouling. Thus, periodic membrane cleaning with chemicals (e.g., acids, bases, surfactants, chelating agents) remains critical to maintaining the long-term membrane performance[207,208]. Lastly, surface modifications have also been widely investigated for membrane fouling mitigation. The two general strategies for surface modifications are (1) to make the membrane surface more hydrophilic which is believed to reduce the adhesion of substances (especially organics and microbes) to the membrane surface[209], or (2) to incorporate microbicidal substances to the membrane surface for biofouling control[200]. Membranes with stronger fouling resistance may reduce the level of pretreatment and frequency of membrane cleaning. Despite a large volume of literature, it is unclear if surface modification is widely adopted in commercial TFC-PA membrane fabrication.

[H1] Outlook

PMD has transformed desalination in the last several decades to become an economically viable process for augmenting freshwater supply and is expected to play an increasingly important role in the 21st century in the face of growing regional water scarcity due to climate change. For municipal-scale desalination of seawater, brackish water, and treated wastewater (for portable reuse), PMD has intrinsic advantages in energy efficiency, operational simplicity, and process reliability. In fact, the energy consumption of SWRO is not too far from the thermodynamic limit so that dramatic energy efficiency improvements as once enabled by the advent of TFC-PA membrane and ERD are no longer possible. So, the question arises: What are (and are not) the next steps for pressure-driven membrane desalination?

Developing membranes with high water permeability, despite being the motivation of many studies on membrane fabrication, will only have marginal contribution to further reducing the energy consumption and LCOW for SWRO. The diminishing return of increasing water permeability for SWRO is attributable to (1) limited saving in applied pressure due to the dominance of osmotic pressure difference over membrane resistance in their contributions to the required pressure, (2) limited flux enhancement due to CP, and (3) membrane cost being a small contribution to the LCOW for SWRO. For low-pressure PMD applications, the benefits of developing highly permeable membranes may be more pronounced but must be justified based on LCOW analysis. Rather than focusing on water permeability, practical RO processes can benefit from developing membranes with higher selectivity toward the removal of small neutral solutes (e.g., boron, 1,4-dioxane, DBPs) and with higher resistances against chlorination and different types of fouling. These improvements will lead to a higher performance stability and/or simplified treatment train which in turn result in a lower LCOW.

Innovations in system configuration play an important role in further improving the efficiency, reliability, and applicability of PMD. One recent example of such innovation is CCRO which has demonstrated advantages for achieving higher WR in BWRO with substantially reduced fouling. Innovations in system configuration are particularly promising when it comes to pushing RO for concentrating high TDS brines. We expect that HPRP and RO variants (LSSRO, OARO, COMRO) will continue to be developed in the next decade to advance RO technology for brine treatment to the next level.

Beyond improving membrane performance and designing new system configurations, future work on PMD should continue to advance our fundamental understanding of mass transport through membranes. Better mass transport theories can help us extract intrinsic parameters for membrane performance evaluation and comparison. It will also help us perform more accurate module-scale modeling for process development and optimization.

Acknowledgement

S. L. and W. L. acknowledges the US-Israel Binational Agricultural Research and Development Fund (Grant No. IS- 5209-19). M. E. acknowledges the Israel-US Collaborative Water-Energy Research Center (Israel-US CoWERC) via Binational Industrial Research and Development Foundation (BIRD) Energy Center Grant EC-15.

Contributions

Introduction (R. E., M.E.); Experimentation (W.L, J. L., and S. L.); Results (W.L, J. L., L. W., Z.W., M. E., R.E., and S. L.); Applications (W. L., M. d. C., S. A. Y., and Z.W.); Reproducibility and data deposition (L. W. and S. L.); Limitations and optimizations (W. L, L. W., and Z. W.); Outlook (R. E., M. E., and S. L.). All authors contributed to reviewing and editing the manuscript.

Competing interests

The authors declare no competing interests.

Related links

Open membrane database： https://openmembranedatabase.org

Glossary

Reverse osmosis

A membrane-based separation process where a hydraulic pressure is applied to push water through a semipermeable membrane that rejects the solutes.

Nanofiltration

A membrane-based separation process similar to RO but with larger membrane pores, higher water flux, and lower solute rejection.

Interfacial polymerization

A polymerization reaction to form a thin film at the interface between two immiscible liquids.

Concentration polarization

A build-up in concentration near membrane surface due to convective transport of solute rejected by the membrane.

References

1. Elimelech, M. & Phillip, W. A. The Future of Seawater Desalination: Energy, Technology, and the Environment. *Science* **333**, 712–717 (2011).
2. Loeb, S. & Sourirajan, S. Sea Water Demineralization by Means of an Osmotic Membrane. in *Saline Water Conversion—II* vol. 38 117–132 (1963).
3. Cadotte, J. E., Petersen, R. J., Larson, R. E. & Erickson, E. E. A new thin-film composite seawater reverse osmosis membrane. *Desalination* **32**, 25–31 (1980).
4. Lu, X. & Elimelech, M. Fabrication of desalination membranes by interfacial polymerization: history, current efforts, and future directions. *Chem Soc Rev* **50**, 6290–6307 (2021).
   This article provides a comprehensive review on the fabrication and characterization of thin-film composite polyamide membranes.

5. Mohammad, A. W. *et al.* Nanofiltration membranes review: Recent advances and future prospects. *Desalination* **356**, 226–254 (2015).
6. Spiegler, K. S. & El-Sayed, Y. M. The energetics of desalination processes. *Desalination* **134**, 109–128 (2001).
7. Greenlee, L. F., Lawler, D. F., Freeman, B. D., Marrot, B. & Moulin, P. Reverse osmosis desalination: Water sources, technology, and today's challenges. *Water Res* **43**, 2317–2348 (2009).
8. Semiat, R. Energy Issues in Desalination Processes. *Environ Sci Technol* **42**, 8193–8201 (2008).
9. Lin, S. Energy Efficiency of Desalination: Fundamental Insights from Intuitive Interpretation. *Environ Sci Technol* **54**, 76–84 (2019).
   This article presents an analysis to show why pressure-driven membrane desalination is intrinsically energy efficient.

10. R. Werber, J., Deshmukh, A. & Elimelech, M. The Critical Need for Increased Selectivity, Not Increased Water Permeability, for Desalination Membranes. *Environ Sci Technol Lett* **3**, 112–120 (2016).
11. Verbeke, R., Gómez, V. & Vankelecom, I. F. J. Chlorine-resistance of reverse osmosis (RO) polyamide membranes. *Prog Polym Sci* **72**, 1–15 (2017).
12. Jiang, S., Li, Y. & Ladewig, B. P. A review of reverse osmosis membrane fouling and control strategies. *Science of The Total Environment* **595**, 567–583 (2017).
13. Davenport, D. M., Deshmukh, A., R. Werber, J. & Elimelech, M. High-Pressure Reverse Osmosis for Energy-Efficient Hypersaline Brine Desalination: Current Status, Design Considerations, and Research Needs. *Environ Sci Technol Lett* **5**, 467–475 (2018).

14. Werber, J. R., Osuji, C. O. & Elimelech, M. Materials for next-generation desalination and water purification membranes. *Nat Rev Mater* **1**, 16018 (2016).

15. Verbeke, R. *et al.* Chlorine-Resistant Epoxide-Based Membranes for Sustainable Water Desalination. *Environ Sci Technol Lett* **8**, 818–824 (2021).

16. Wang, Z., Deshmukh, A., Du, Y. & Elimelech, M. Minimal and zero liquid discharge with reverse osmosis using low-salt-rejection membranes. *Water Res* **170**, 115317 (2020).

17. Nativ, P., Leifman, O., Lahav, O. & Epsztein, R. Desalinated brackish water with improved mineral composition using monovalent-selective nanofiltration followed by reverse osmosis. *Desalination* **520**, 115364 (2021).

18. Ismail, A. F. & Matsuura, T. Progress in transport theory and characterization method of Reverse Osmosis (RO) membrane in past fifty years. *Desalination* **434**, 2–11 (2018).

19. Geise, G. M., Paul, D. R. & Freeman, B. D. Fundamental water and salt transport properties of polymeric materials. *Prog Polym Sci* **39**, 1–42 (2014).

20. Wijmans, J. G. & Baker, R. W. The solution-diffusion model: a review. *J Memb Sci* **107**, 1–21 (1995).

21. Heiranian, M., M. DuChanois, R., L. Ritt, C., Violet, C. & Elimelech, M. Molecular Simulations to Elucidate Transport Phenomena in Polymeric Membranes. *Environ Sci Technol* **56**, 3313–3323 (2022).

22. Faucher, S. *et al.* Critical Knowledge Gaps in Mass Transport through Single-Digit Nanopores: A Review and Perspective. *The Journal of Physical Chemistry C* **123**, 21309–21326 (2019).

23. Lu, C. *et al.* In Situ Characterization of Dehydration during Ion Transport in Polymeric Nanochannels. *J Am Chem Soc* **143**, 14242–14252 (2021).

24. Wang, L. *et al.* Water transport in reverse osmosis membranes is governed by pore flow, not a solution-diffusion mechanism. *Sci Adv* **9**, eadf8488 (2023).

This article reports experimental and simulation-based evidence to support pore flow as the true mechanism for water transport in reverse osmosis membranes.

25. Wang, L. *et al.* Salt and Water Transport in Reverse Osmosis Membranes: Beyond the Solution-Diffusion Model. *Environ Sci Technol* **55**, 16665–16675 (2021).

This article introduces a new solution-friction framework for modeling water and salt transport in reverse osmosis membranes.

26. Zhou, X. *et al.* Intrapore energy barriers govern ion transport and selectivity of desalination membranes. *Sci Adv* **6**, eabd9045 (2023).

27. Epsztein, R., DuChanois, R. M., Ritt, C. L., Noy, A. & Elimelech, M. Towards single-species selectivity of membranes with subnanometre pores. *Nat Nanotechnol* **15**, 426–436 (2020).

28. Aluru, N. R. *et al.* Fluids and Electrolytes under Confinement in Single-Digit Nanopores. *Chem Rev* **123**, 2737–2831 (2023).

29. Lee, K. P., Arnot, T. C. & Mattia, D. A review of reverse osmosis membrane materials for desalination—Development to date and future potential. *J Memb Sci* **370**, 1–22 (2011).

30. Song, Y., Sun, P., Henry, L. L. & Sun, B. Mechanisms of structure and performance controlled thin film composite membrane formation via interfacial polymerization process. *J Memb Sci* **251**, 67–79 (2005).

31. Freger, V. & Ramon, G. Z. Polyamide desalination membranes: Formation, structure, and properties. *Prog Polym Sci* **122**, 101451 (2021).
32. Chai, G. Y. & Krantz, W. B. Formation and characterization of polyamide membranes via interfacial polymerization. *J Memb Sci* **93**, 175–192 (1994).
33. Nowbahar, A. *et al.* Measuring Interfacial Polymerization Kinetics Using Microfluidic Interferometry. *J Am Chem Soc* **140**, 3173–3176 (2018).
34. Freger, V. Nanoscale Heterogeneity of Polyamide Membranes Formed by Interfacial Polymerization. *Langmuir* **19**, 4791–4797 (2003).
35. Xie, W. *et al.* Polyamide interfacial composite membranes prepared from m-phenylene diamine, trimesoyl chloride and a new disulfonated diamine. *J Memb Sci* **403–404**, 152–161 (2012).
36. Li, L., Zhang, S., Zhang, X. & Zheng, G. Polyamide thin film composite membranes prepared from isomeric biphenyl tetraacyl chloride and m-phenylenediamine. *J Memb Sci* **315**, 20–27 (2008).
37. Yao, Y. *et al.* High performance polyester reverse osmosis desalination membrane with chlorine resistance. *Nat Sustain* **4**, 138–146, (2021).
38. Ghosh, A. K., Jeong, B. H., Huang, X. & Hoek, E. M. V. Impacts of reaction and curing conditions on polyamide composite reverse osmosis membrane properties. *J Memb Sci* **311**, 34–45 (2008).
39. Liang, Y. *et al.* Polyamide nanofiltration membrane with highly uniform sub-nanometre pores for sub-1 Å precision separation. *Nat Commun* **11**, 1–9 (2020).
40. Lu, Y. *et al.* Two-dimensional fractal nanocrystals templating for substantial performance enhancement of polyamide nanofiltration membrane. *Proceedings of the National Academy of Sciences* **118**, e2019891118 (2021).
41. Khorshidi, B., Thundat, T., Pernitsky, D. & Sadrzadeh, M. A parametric study on the synergistic impacts of chemical additives on permeation properties of thin film composite polyamide membrane. *J Memb Sci* **535**, 248–257 (2017).
42. Mansourpanah, Y., Madaeni, S. S. & Rahimpour, A. Fabrication and development of interfacial polymerized thin-film composite nanofiltration membrane using different surfactants in organic phase; study of morphology and performance. *J Memb Sci* **343**, 219–228 (2009).
43. Elfa Peng, L., Yao, Z., Yang, Z., Guo, H. & Y. Tang, C. Dissecting the Role of Substrate on the Morphology and Separation Properties of Thin Film Composite Polyamide Membranes: Seeing Is Believing. *Environ Sci Technol* **54**, 6978–6986 (2020).
44. Karan, S., Jiang, Z. & Livingston, A. G. Sub–10 nm polyamide nanofilms with ultrafast solvent transport for molecular separation. *Science* **348**, 1347–1351 (2015).
45. Ma, X. H. *et al.* Nanofoaming of Polyamide Desalination Membranes to Tune Permeability and Selectivity. *Environ Sci Technol Lett* **5**, 123–130 (2018).
46. Gao, S. *et al.* Ultrathin Polyamide Nanofiltration Membrane Fabricated on Brush-Painted Single-Walled Carbon Nanotube Network Support for Ion Sieving. *ACS Nano* **13**, 5278–5290 (2019).
47. Dai, R., Li, J. & Wang, Z. Constructing interlayer to tailor structure and performance of thin-film composite polyamide membranes: A review. *Adv Colloid Interface Sci* **282**, 102204 (2020).

48. Shao, S. *et al.* Nanofiltration Membranes with Crumpled Polyamide Films: A Critical Review on Mechanisms, Performances, and Environmental Applications. *Environ Sci Technol* **56**, 12811–12827 (2022).
49. Yang, Z., Guo, H. & Tang, C. Y. The upper bound of thin-film composite (TFC) polyamide membranes for desalination. *J Memb Sci* **590**, 117297 (2019).
This article provides a review on quantifying the performance of thin-film composite polyamide membranes based on the solution-diffusion theory.

50. Peng, L. E. *et al.* A critical review on porous substrates of TFC polyamide membranes: Mechanisms, membrane performances, and future perspectives. *J Memb Sci* **641**, 119871 (2022).
51. Chowdhury, M. R., Steffes, J., Huey, B. D. & McCutcheon, J. R. 3D printed polyamide membranes for desalination. *Science* **361**, 682–686 (2018).
52. Kang, Y. *et al.* PIP/TMC Interfacial Polymerization with Electrospray: Novel Loose Nanofiltration Membrane for Dye Wastewater Treatment. *ACS Appl Mater Interfaces* **12**, 36148–36158 (2020).
53. He, J. *et al.* Molecular mechanisms of thickness-dependent water desalination in polyamide reverse-osmosis membranes. *J Memb Sci* **674**, 121498 (2023).
54. Ma, X.-H. *et al.* Interfacial Polymerization with Electrosprayed Microdroplets: Toward Controllable and Ultrathin Polyamide Membranes. *Environ Sci Technol Lett* **5**, 117–122 (2018).
55. J. Harris, J., M. DeRose, P. & L. Bruening, M. Synthesis of Passivating, Nylon-Like Coatings through Cross-Linking of Ultrathin Polyelectrolyte Films. *J Am Chem Soc* **121**, 1978–1979 (1999).
56. Liang, Y. & Lin, S. Mechanism of Permselectivity Enhancement in Polyelectrolyte-Dense Nanofiltration Membranes via Surfactant-Assembly Intercalation. *Environ Sci Technol* **55**, 738–748 (2020).
57. DuChanois, R. M., Epsztein, R., Trivedi, J. A. & Elimelech, M. Controlling pore structure of polyelectrolyte multilayer nanofiltration membranes by tuning polyelectrolyte-salt interactions. *J Memb Sci* **581**, 413–420 (2019).
58. Gu, J.-E. *et al.* Molecular Layer-by-Layer Assembled Thin-Film Composite Membranes for Water Desalination. *Advanced Materials* **25**, 4778–4782 (2013).
59. Jin, W., Toutianoush, A. & Tieke, B. Use of Polyelectrolyte Layer-by-Layer Assemblies as Nanofiltration and Reverse Osmosis Membranes. *Langmuir* **19**, 2550–2553 (2003).
60. Song, X. *et al.* Intrinsic Nanoscale Structure of Thin Film Composite Polyamide Membranes: Connectivity, Defects, and Structure–Property Correlation. *Environ Sci Technol* **54**, 3559–3569 (2020).
61. Pacheco, F. A., Pinnau, I., Reinhard, M. & Leckie, J. O. Characterization of isolated polyamide thin films of RO and NF membranes using novel TEM techniques. *J Memb Sci* **358**, 51–59 (2010).
62. Tan, Z., Chen, S., Peng, X., Zhang, L. & Gao, C. Polyamide membranes with nanoscale Turing structures for water purification. *Science* **360**, 518–521 (2018).
63. Guo, H. *et al.* A One-Step Rapid Assembly of Thin Film Coating Using Green Coordination Complexes for Enhanced Removal of Trace Organic Contaminants by Membranes. *Environ Sci Technol* **51**, 12638–12643 (2017).

64. Ren, Y. *et al.* High flux thin film nanocomposite membranes based on porous organic polymers for nanofiltration. *J Memb Sci* **585**, 19–28 (2019).
65. Wang, F. *et al.* Enhanced Water Permeability and Antifouling Property of Coffee-Ring-Textured Polyamide Membranes by In Situ Incorporation of a Zwitterionic Metal–Organic Framework. *Environ Sci Technol* **55**, 5324–5334 (2021).
66. Kłosowski, M. M. *et al.* Micro-to nano-scale characterisation of polyamide structures of the SW30HR RO membrane using advanced electron microscopy and stain tracers. *J Memb Sci* **520**, 465–476 (2016).
67. Lu, X. *et al.* Elements Provide a Clue: Nanoscale Characterization of Thin-Film Composite Polyamide Membranes. *ACS Appl Mater Interfaces* **7**, 16917–16922 (2015).
68. Tang, C. Y., Kwon, Y. N. & Leckie, J. O. Effect of membrane chemistry and coating layer on physiochemical properties of thin film composite polyamide RO and NF membranes: II. Membrane physiochemical properties and their dependence on polyamide and coating layers. *Desalination* **242**, 168–182 (2009).
69. Hilal, N., Al-Zoubi, H., Darwish, N. A. & Mohammad, A. W. Characterisation of nanofiltration membranes using atomic force microscopy. *Desalination* **177**, 187–199 (2005).
70. Culp, T. E. *et al.* Nanoscale control of internal inhomogeneity enhances water transport in desalination membranes. *Science* **371**, 72–75 (2021).
71. Culp, T. E. *et al.* Electron tomography reveals details of the internal microstructure of desalination membranes. *Proceedings of the National Academy of Sciences* **115**, 8694–8699 (2018).
72. Pacheco, F., Sougrat, R., Reinhard, M., Leckie, J. O. & Pinnau, I. 3D visualization of the internal nanostructure of polyamide thin films in RO membranes. *J Memb Sci* **501**, 33–44 (2016).
73. Hung, W.-S. *et al.* Non-destructive means of probing a composite polyamide membrane for characteristic free volume, void, and chemical composition. *RSC Adv* **6**, 85019–85025 (2016).
74. Chen, H. *et al.* Free-Volume Depth Profile of Polymeric Membranes Studied by Positron Annihilation Spectroscopy: Layer Structure from Interfacial Polymerization. *Macromolecules* **40**, 7542–7557 (2007).
75. Li, T., J. Senesi, A. & Lee, B. Small Angle X-ray Scattering for Nanoparticle Research. *Chem Rev* **116**, 11128–11180 (2016).
76. Mahmood, A. & Wang, J.-L. A Review of Grazing Incidence Small- and Wide-Angle X-Ray Scattering Techniques for Exploring the Film Morphology of Organic Solar Cells. *Solar RRL* **4**, 2000337 (2020).
77. Fu, Q. *et al.* Molecular Structure of Aromatic Reverse Osmosis Polyamide Barrier Layers. *ACS Macro Lett* **8**, 352–356 (2019).
78. Singh, P. S., Ray, P., Xie, Z. & Hoang, M. Synchrotron SAXS to probe cross-linked network of polyamide ‘reverse osmosis’ and ‘nanofiltration’ membranes. *J Memb Sci* **421–422**, 51–59 (2012).
79. Ho Kim, S., Kwak, S.-Y. & Suzuki, T. Positron Annihilation Spectroscopic Evidence to Demonstrate the Flux-Enhancement Mechanism in Morphology-Controlled Thin-Film-Composite (TFC) Membrane. *Environ Sci Technol* **39**, 1764–1770 (2005).
80. Hilal, N., Ismail, A. F., Matsuura, T. & Oatley-Radcliffe, D. *Membrane characterization.* (Elsevier, 2017).

This book introduces the various experimental techniques for membrane characterizations.

81. Ben-David, A., Oren, Y. & Freger, V. Thermodynamic Factors in Partitioning and Rejection of Organic Compounds by Polyamide Composite Membranes. *Environ Sci Technol* **40**, 7023–7028 (2006).
82. Zhu, M. M. *et al.* Antifouling and antibacterial behavior of membranes containing quaternary ammonium and zwitterionic polymers. *J Colloid Interface Sci* **584**, 225–235 (2021).
83. García-Martín, N. *et al.* Pore size analysis from retention of neutral solutes through nanofiltration membranes. The contribution of concentration–polarization. *Desalination* **344**, 1–11 (2014).
84. Fetters, L. J., Hadjichristidis, N., Lindner, J. S. & Mays, J. W. Molecular Weight Dependence of Hydrodynamic and Thermodynamic Properties for Well-Defined Linear Polymers in Solution. *J Phys Chem Ref Data* **23**, 619–640 (1994).
85. Lee, H., Venable, R. M., MacKerell Jr., A. D. & Pastor, R. W. Molecular Dynamics Studies of Polyethylene Oxide and Polyethylene Glycol: Hydrodynamic Radius and Shape Anisotropy. *Biophys J* **95**, 1590–1599 (2008).
86. Wang, R. & Lin, S. Pore model for nanofiltration: History, theoretical framework, key predictions, limitations, and prospects. *J Memb Sci* **620**, 118809 (2021).
This article provides a comprehensive review summarizing theoretical framework, procedure of implementation, and limitations of the Donnan Steric Pore Model with Dielectric Exclusion (DSPM-DE)

87. Bowen, W. R., Mohammad, A. W. & Hilal, N. Characterisation of nanofiltration membranes for predictive purposes — use of salts, uncharged solutes and atomic force microscopy. *J Memb Sci* **126**, 91–105 (1997).
88. Tang, C. Y., Kwon, Y. N. & Leckie, J. O. Probing the nano- and micro-scales of reverse osmosis membranes—A comprehensive characterization of physiochemical properties of uncoated and coated membranes by XPS, TEM, ATR-FTIR, and streaming potential measurements. *J Memb Sci* **287**, 146–156 (2007).
89. Chastain, J. & King Jr, R. C. *Handbook of X-ray photoelectron spectroscopy*. *Perkin-Elmer Corporation* vol. 40 (Perkin-Elmer Corporation, 1992).
90. Tang, C. Y., Kwon, Y. N. & Leckie, J. O. Effect of membrane chemistry and coating layer on physiochemical properties of thin film composite polyamide RO and NF membranes: I. FTIR and XPS characterization of polyamide and coating layer chemistry. *Desalination* **242**, 149–167 (2009).
91. Zimudzi, T. J. *et al.* Quantifying carboxylic acid concentration in model polyamide desalination membranes via Fourier transform infrared spectroscopy. *Macromolecules* **51**, 6623–6629 (2018).
92. Freger, V. *et al.* Characterization of novel acid-stable NF membranes before and after exposure to acid using ATR-FTIR, TEM and AFM. *J Memb Sci* **256**, 134–142 (2005).
93. Nikkola, J. *et al.* Surface modification of thin film composite RO membrane for enhanced anti-biofouling performance. *J Memb Sci* **444**, 192–200 (2013).

94. Zhou, S. *et al.* Unveiling the Growth of Polyamide Nanofilms at Water/Organic Free Interfaces: Toward Enhanced Water/Salt Selectivity. *Environ Sci Technol* **56**, 10279–10288 (2022).
95. Chen, D., Werber, J. R., Zhao, X. & Elimelech, M. A facile method to quantify the carboxyl group areal density in the active layer of polyamide thin-film composite membranes. *J Memb Sci* **534**, 100–108 (2017).
96. Ritt, C. L. *et al.* Ionization behavior of nanoporous polyamide membranes. *Proceedings of the National Academy of Sciences* **117**, 30191–30200 (2020).
97. Tiraferri, A. & Elimelech, M. Direct quantification of negatively charged functional groups on membrane surfaces. *J Memb Sci* **389**, (2012).
98. Perry, L. A. & Coronell, O. Reliable, bench-top measurements of charge density in the active layers of thin-film composite and nanocomposite membranes using quartz crystal microbalance technology. *J Memb Sci* **429**, 23–33 (2013).
99. Coronell, O., J. Mariñas, B., Zhang, X. & G. Cahill, D. Quantification of Functional Groups and Modeling of Their Ionization Behavior in the Active Layer of FT30 Reverse Osmosis Membrane. *Environ Sci Technol* **42**, 5260–5266 (2008).
100. Möckel, D., Staude, E., Dal-Cin, M., Darcovich, K. & Guiver, M. Tangential flow streaming potential measurements: Hydrodynamic cell characterization and zeta potentials of carboxylated polysulfone membranes. *J Memb Sci* **145**, 211–222 (1998).
101. Hurwitz, G., Guillen, G. R. & Hoek, E. M. V. Probing polyamide membrane surface charge, zeta potential, wettability, and hydrophilicity with contact angle measurements. *J Memb Sci* **349**, 349–357 (2010).
102. Elimelech, M. & O'Melia, C. R. Effect of electrolyte type on the electrophoretic mobility of polystyrene latex colloids. *Colloids and Surfaces* **44**, (1990).
103. Childress, A. E. & Elimelech, M. Effect of solution chemistry on the surface charge of polymeric reverse osmosis and nanofiltration membranes. *J Memb Sci* **119**, 253–268 (1996).
104. Xu, P. *et al.* Positive charged PEI-TMC composite nanofiltration membrane for separation of Li+ and Mg2+ from brine with high Mg2+/Li+ ratio. *Desalination* **449**, 57–68 (2019).
105. Ismail, M. F., Islam, M. A., Khorshidi, B., Tehrani-Bagha, A. & Sadrzadeh, M. Surface characterization of thin-film composite membranes using contact angle technique: Review of quantification strategies and applications. *Adv Colloid Interface Sci* **299**, 102524 (2022).
106. Li, S. L., Wu, P., Wang, J., Wang, J. & Hu, Y. Fabrication of high performance polyamide reverse osmosis membrane from monomer 4-morpholino-m-phenylenediamine and tailoring with zwitterions. *Desalination* **473**, 114169 (2020).
107. Zhang, Y. *et al.* Surface modification of polyamide reverse osmosis membrane with sulfonated polyvinyl alcohol for antifouling. *Appl Surf Sci* **419**, 177–187 (2017).
108. Liu, C. *et al.* An outstanding antichlorine and antibacterial membrane with quaternary ammonium salts of alkenes via in situ polymerization for textile wastewater treatment. *Chemical Engineering Journal* **384**, 123306 (2020).
109. Ismail, M. F., Khorshidi, B. & Sadrzadeh, M. New insights into the impact of nanoscale surface heterogeneity on the wettability of polymeric membranes. *J Memb Sci* **590**, 117270 (2019).
110. Van der Bruggen, B. Microfiltration, ultrafiltration, nanofiltration, reverse osmosis, and forward osmosis. *Fundamental Modeling of Membrane Systems: Membrane and Process Performance* 25–70 (2018).

111. Tansel, B. *et al.* Significance of hydrated radius and hydration shells on ionic permeability during nanofiltration in dead end and cross flow modes. *Sep Purif Technol* **51**, 40–47 (2006).

112. Davenport, D. M. *et al.* Thin film composite membrane compaction in high-pressure reverse osmosis. *J Memb Sci* **610**, 118268 (2020).

113. Zydney, A. L. Stagnant film model for concentration polarization in membrane systems. *J Memb Sci* **130**, 275–281 (1997).

114. Sablani, S., Goosen, M., Al-Belushi, R. & Wilf, M. Concentration polarization in ultrafiltration and reverse osmosis: a critical review. *Desalination* **141**, 269–289 (2001).

115. Gao, H. *et al.* Revolutionizing Membrane Design Using Machine Learning-Bayesian Optimization. *Environ Sci Technol* **56**, 2572–2581 (2022).

116. Ritt, C. L. *et al.* The open membrane database: Synthesis–structure–performance relationships of reverse osmosis membranes. *J Memb Sci* **641**, 119927 (2022).
This article introduces the Open Membrane Database (OMD) which is a web-based platform for data depository and analysis: https://openmembranedatabase.org

117. Mai, Z. *et al.* Activity-derived model for water and salt transport in reverse osmosis membranes: A combination of film theory and electrolyte theory. *Desalination* **469**, 114094 (2019).

118. Biesheuvel, P. M., Rutten, S. B., Ryzhkov, I. I., Porada, S. & Elimelech, M. Theory for salt transport in charged reverse osmosis membranes: Novel analytical equations for desalination performance and experimental validation. *Desalination* **557**, 116580 (2023).
This article reports a new set of analytical equations to describe the transport of a single salt in reverse osmosis derived based on the solution-friction framework.

119. Oren, Y. S. & Biesheuvel, P. M. Theory of ion and water transport in reverse-osmosis membranes. *Phys Rev Appl* **9**, 24034 (2018).

120. Wang, L. *et al.* Significance of Co-ion Partitioning in Salt Transport through Polyamide Reverse Osmosis Membranes. *Environ Sci Technol* **57**, 3930–3939 (2023).

121. Yaroshchuk, A., Bruening, M. L. & Licón Bernal, E. E. Solution-Diffusion–Electro-Migration model and its uses for analysis of nanofiltration, pressure-retarded osmosis and forward osmosis in multi-ionic solutions. *J Memb Sci* **447**, 463–476 (2013).
This article introduces the solution-diffusion-electromigration (SDEM) model which can be used for analyzing transport of multiple ion species.

122. Yaroshchuk, A. & Bruening, M. L. An analytical solution of the solution-diffusion-electromigration equations reproduces trends in ion rejections during nanofiltration of mixed electrolytes. *J Memb Sci* **523**, 361–372 (2017).

123. Wang, R., He, R., He, T., Elimelech, M. & Lin, S. Performance metrics for nanofiltration-based selective separation for resource extraction and recovery. *Nature Water* **1**, 291–300 (2023).

124. Bowen, W. R. & Welfoot, J. S. Modelling the performance of membrane nanofiltration—critical assessment and model development. *Chem Eng Sci* **57**, 1121–1137 (2002).

125. Rehman, D. & Lienhard, J. H. Global optimization for accurate and efficient parameter estimation in nanofiltration. *Journal of Membrane Science Letters* **2**, 100034 (2022).

126. Liang, Y., Dudchenko, A. V. & Mauter, M. S. Novel method for accurately estimating membrane transport properties and mass transfer coefficients in reverse osmosis. *J Memb Sci* **679**, 121686 (2023).

Both Ref. 125 and 126 report a similar approach of model parameter determination based on minimizing global error.

127. Biesheuvel, P.M., Porada, S., Elimelech, M., Dykstra, D.E., Tutorial review of reverse osmosis and electrodialysis, *J Memb Sci* **647**, 120221 (2023).

128. Schwinge, J., Neal, P. R., Wiley, D. E., Fletcher, D. F. & Fane, A. G. Spiral wound modules and spacers: Review and analysis. *J Memb Sci* **242**, 129–153 (2004).

129. Roy, Y., Sharqawy, M. H. & Lienhard, J. H. Modeling of flat-sheet and spiral-wound nanofiltration configurations and its application in seawater nanofiltration. *J Memb Sci* **493**, 360–372 (2015).

130. Elimelech, M. & Phillip, W. A. The future of seawater desalination: energy, technology, and the environment. *Science* **333**, 712–717 (2011).

131. Lin, S. & Elimelech, M. Staged reverse osmosis operation: Configurations, energy efficiency, and application potential. *Desalination* **366**, 9–14 (2015).

132. Warsinger, D. M., Tow, E. W., Nayar, K. G., Maswadeh, L. A. & Lienhard V, J. H. Energy efficiency of batch and semi-batch (CCRO) reverse osmosis desalination. *Water Res* **106**, 272–282 (2016).

133. Quon, H. *et al.* Pipe Parity Analysis of Seawater Desalination in the United States: Exploring Costs, Energy, and Reliability via Case Studies and Scenarios of Emerging Technology. *ACS ES&T Engineering* **2**, 434–445 (2021).

134. Okamoto, Y. & Lienhard, J. H. How RO membrane permeability and other performance factors affect process cost and energy use: A review. *Desalination* **470**, 114064 (2019).

135. GWI, DesalData. www.desaldata.com.

136. Kim, J., Park, K., Yang, D. R. & Hong, S. A comprehensive review of energy consumption of seawater reverse osmosis desalination plants. *Appl Energy* **254**, 113652 (2019).

137. Sauvet-Goichon, B. Ashkelon desalination plant — A successful challenge. *Desalination* **203**, 75–81 (2007).

138. Hermony, A., Sutzkover-Gutman, I., Talmi, Y. & Fine, O. Palmachim Seawater desalination plant—seven years of expansions with uninterrupted operation together with process improvements. *Desalination Water Treat* **55**, 2526–2535 (2015).

139. Okamoto, Y. & Lienhard, J. H. How RO membrane permeability and other performance factors affect process cost and energy use: A review. *Desalination* **470**, 114064 (2019).

140. Voutchkov, N. Energy use for membrane seawater desalination – current status and trends. *Desalination* **431**, 2–14 (2018).

141. Amy, G. *et al.* Membrane-based seawater desalination: Present and future prospects. *Desalination* **401**, 16–21 (2017).

142. Voutchkov, N. Energy use for membrane seawater desalination – current status and trends. *Desalination* **431**, 2–14 (2018).

143. Sorek II Desalination Plant (Israel). *IDE Tech. https://ide-tech.com/en/project/sorek-b-desalination-plant/.*

144. Xu, X. *et al.* Analysis of Brackish Water Desalination for Municipal Uses: Case Studies on Challenges and Opportunities. *ACS ES&T Engineering* **2**, 306–322 (2022).

145. Jones, E., Qadir, M., van Vliet, M. T. H., Smakhtin, V. & Kang, S. mu. The state of desalination and brine production: A global outlook. *Science of The Total Environment* **657**, 1343–1356 (2019).

146. Pan, S. Y., Haddad, A. Z., Kumar, A. & Wang, S. W. Brackish water desalination using reverse osmosis and capacitive deionization at the water-energy nexus. *Water Res* **183**, 116064 (2020).

147. Mogheir, Y., Foul, A. A., Abuhabib, A. A. & Mohammad, A. W. Assessment of large scale brackish water desalination plants in the Gaza Strip. *Desalination* **314**, 96–100 (2013).

148. Mickley, M. Updated and extended survey of US municipal desalination plants. *Desalination and Water Purification Research and Development Program Report* (2018).

149. Almulla, A., Eid, M., Côté, P. & Coburn, J. Developments in high recovery brackish water desalination plants as part of the solution to water quantity problems. *Desalination* **153**, 237–243 (2003).

150. Karime, M., Bouguecha, S. & Hamrouni, B. RO membrane autopsy of Zarzis brackish water desalination plant. *Desalination* **220**, 258–266 (2008).

151. K. Patel, S., Maarten Biesheuvel, P. & Elimelech, M. Energy Consumption of Brackish Water Desalination: Identifying the Sweet Spots for Electrodialysis and Reverse Osmosis. *ACS ES&T Engineering* **1**, 851–864 (2021).

152. Liu, X., Shanbhag, S., V. Bartholomew, T., F. Whitacre, J. & S. Mauter, M. Cost Comparison of Capacitive Deionization and Reverse Osmosis for Brackish Water Desalination. *ACS ES&T Engineering* **1**, 261–273 (2020).

153. Drak, A. & Adato, M. Energy recovery consideration in brackish water desalination. *Desalination* **339**, 34–39 (2014).

154. Global Water Intelligence. *The IDA – Desalination & Reuse Handbook 2022-2023*.

155. E. Giammar, D. *et al.* Cost and Energy Metrics for Municipal Water Reuse. *ACS ES&T Engineering* **2**, 489–507 (2021).

156. Metcalf & Eddy, Inc. an A. C., Asano, T., Burton, F. & Leverenz, H. Water Reuse Technologies and Treatment Systems: An Overview. in *Water Reuse: Issues, Technologies, and Applications* (McGraw-Hill Education, 2007).

157. L. Marron, E., A. Mitch, W., von Gunten, U. & L. Sedlak, D. A Tale of Two Treatments: The Multiple Barrier Approach to Removing Chemical Contaminants During Potable Water Reuse. *Acc Chem Res* **52**, 615–622 (2019).

158. Warsinger, D. M. *et al.* A review of polymeric membranes and processes for potable water reuse. *Prog Polym Sci* **81**, 209–237 (2018).

159. Tow, E. W. *et al.* Modeling the energy consumption of potable water reuse schemes. *Water Res X* **13**, 100126 (2021).

160. Sim, A. & Mauter, M. S. Cost and energy intensity of US potable water reuse systems. *Environ Sci (Camb)* **7**, 748–761 (2021).

161. Grant, S. B. *et al.* Taking the 'waste' out of 'wastewater' for human water security and ecosystem sustainability. *Science* vol. 337 Preprint at https://doi.org/10.1126/science.1216852 (2012).

162. Tong, T. & Elimelech, M. The Global Rise of Zero Liquid Discharge for Wastewater Management: Drivers, Technologies, and Future Directions. *Environ Sci Technol* **50**, 6846–6855 (2016).

163. Davenport, D. M., Deshmukh, A., R. Werber, J. & Elimelech, M. High-Pressure Reverse Osmosis for Energy-Efficient Hypersaline Brine Desalination: Current Status, Design Considerations, and Research Needs. *Environ Sci Technol Lett* **5**, 467–475 (2018).
164. Davenport, D. M., Wang, L., Shalusky, E. & Elimelech, M. Design principles and challenges of bench-scale high-pressure reverse osmosis up to 150 bar. *Desalination* **517**, 115237 (2021).
165. Chen, X. & Yin Yip, N. Unlocking High-Salinity Desalination with Cascading Osmotically Mediated Reverse Osmosis: Energy and Operating Pressure Analysis. *Environ Sci Technol* **52**, 2242–2250 (2018).
166. Bartholomew, T. V., Mey, L., Arena, J. T., Siefert, N. S. & Mauter, M. S. Osmotically assisted reverse osmosis for high salinity brine treatment. *Desalination* **421**, 3–11 (2017).
167. Wang, Z., Deshmukh, A., Du, Y. & Elimelech, M. Minimal and zero liquid discharge with reverse osmosis using low-salt-rejection membranes. *Water Res* **170**, 115317 (2020).
168. Bartholomew, T. V., S. Siefert, N. & S. Mauter, M. Cost Optimization of Osmotically Assisted Reverse Osmosis. *Environ Sci Technol* **52**, 11813–11821 (2018).
169. Wang, Z., Feng, D., Chen, Y., He, D. & Elimelech, M. Comparison of Energy Consumption of Osmotically Assisted Reverse Osmosis and Low-Salt-Rejection Reverse Osmosis for Brine Management. *Environ Sci Technol* **55**, 10714–10723 (2021).
170. Jiang, C. *et al.* Thin-film composite membranes with aqueous template-induced surface nanostructures for enhanced nanofiltration. *J Memb Sci* **589**, (2019).
171. Pranić, M., M. Kimani, E., M. Biesheuvel, P. & Porada, S. Desalination of Complex Multi-Ionic Solutions by Reverse Osmosis at Different pH Values, Temperatures, and Compositions. *ACS Omega* **6**, 19946–19955 (2021).
172. Kimani, E. M. *et al.* The influence of feedwater pH on membrane charge ionization and ion rejection by reverse osmosis: An experimental and theoretical study. *J Memb Sci* **660**, (2022).
173. Applied Membranes Inc. Membrane Performance Factors Temperature Correction. *https://appliedmembranes.com/media/wysiwyg/pdf/membranes/temperature_correction_chart_for_ro_membranes.pdf.*
174. DuPont Water Solutions. FilmTec^{TM} Temperature Correction Factor Technical Manual Excerpt. *https://www.dupont.com/content/dam/dupont/amer/us/en/water-solutions/public/documents/en/RO-NF-FilmTec-Temperature-Correction-Factor-Manual-Exc-45-D01658-en.pdf.*
175. Jamaly, S., Darwish, N. N., Ahmed, I. & Hasan, S. W. A short review on reverse osmosis pretreatment technologies. *Desalination* **354**, 30–38 (2014).
176. Henthorne, L. & Boysen, B. State-of-the-art of reverse osmosis desalination pretreatment. *Desalination* **356**, 129–139 (2015).
177. Kang, G. D. *et al.* Study on hypochlorite degradation of aromatic polyamide reverse osmosis membrane. *J Memb Sci* **300**, 165–171 (2007).
178. Gohil, J. M. & Suresh, A. K. Chlorine attack on reverse osmosis membranes: Mechanisms and mitigation strategies. *J Memb Sci* **541**, 108–126 (2017).
179. Glater, J., Hong, S. kwan & Elimelech, M. The search for a chlorine-resistant reverse osmosis membrane. *Desalination* **95**, 325–345 (1994).
180. Xue, J. *et al.* Chlorine-resistant polyester thin film composite nanofiltration membranes prepared with β-cyclodextrin. *J Memb Sci* **584**, 282–289 (2019).

181. Paul, M. *et al.* Synthesis and crosslinking of partially disulfonated poly(arylene ether sulfone) random copolymers as candidates for chlorine resistant reverse osmosis membranes. *Polymer (Guildf)* **49**, 2243–2252 (2008).

182. Ni, L., Meng, J., Li, X. & Zhang, Y. Surface coating on the polyamide TFC RO membrane for chlorine resistance and antifouling performance improvement. *J Memb Sci* **451**, 205–215 (2014).

183. Du, R. & Zhao, J. Properties of poly (N,N-dimethylaminoethyl methacrylate)/polysulfone positively charged composite nanofiltration membrane. *J Memb Sci* **239**, 183–188 (2004).

184. Hu, Y. *et al.* Enhancing the performance of aromatic polyamide reverse osmosis membrane by surface modification via covalent attachment of polyvinyl alcohol (PVA). *J Memb Sci* **501**, 209–219 (2016).

185. Liu, M., Chen, Q., Wang, L., Yu, S. & Gao, C. Improving fouling resistance and chlorine stability of aromatic polyamide thin-film composite RO membrane by surface grafting of polyvinyl alcohol (PVA). *Desalination* **367**, 11–20 (2015).

186. Jun, B. M. *et al.* Applications of metal-organic framework based membranes in water purification: A review. *Sep Purif Technol* **247**, 116947 (2020).

187. Zhao, H. *et al.* Improving the performance of polyamide reverse osmosis membrane by incorporation of modified multi-walled carbon nanotubes. *J Memb Sci* **450**, 249–256 (2014).

188. Chae, H. R., Lee, J., Lee, C. H., Kim, I. C. & Park, P. K. Graphene oxide-embedded thin-film composite reverse osmosis membrane with high flux, anti-biofouling, and chlorine resistance. *J Memb Sci* **483**, 128–135 (2015).

189. World Health Organization. *Guidelines for drinking-water quality. WHO chronicle* vol. 38 (2011).

190. Shaffer, D. L., Yip, N. Y., Gilron, J. & Elimelech, M. Seawater desalination for agriculture by integrated forward and reverse osmosis: Improved product water quality for potentially less energy. *J Memb Sci* **415–416**, 1–8 (2012).

191. Tu, K. L., Nghiem, L. D. & Chivas, A. R. Boron removal by reverse osmosis membranes in seawater desalination applications. *Separation and Purification Technology* vol. 75 Preprint at https://doi.org/10.1016/j.seppur.2010.07.021 (2010).

192. Hyung, H. & Kim, J.-H. A mechanistic study on boron rejection by sea water reverse osmosis membranes. *J Memb Sci* **286**, 269–278 (2006).

193. Bernstein, R., Belfer, S. & Freger, V. Toward Improved Boron Removal in RO by Membrane Modification: Feasibility and Challenges. *Environ Sci Technol* **45**, 3613–3620 (2011).

194. Linge, K. L. *et al.* Formation of halogenated disinfection by-products during microfiltration and reverse osmosis treatment: Implications for water recycling. *Sep Purif Technol* **104**, (2013).

195. Fujioka, T. *et al.* N-nitrosamine rejection by nanofiltration and reverse osmosis membranes: The importance of membrane characteristics. *Desalination* **316**, 67–75 (2013).

196. Malaeb, L. & Ayoub, G. M. Reverse osmosis technology for water treatment: State of the art review. *Desalination* **267**, 1–8 (2011).

197. Jiang, S., Li, Y. & Ladewig, B. P. A review of reverse osmosis membrane fouling and control strategies. *Science of The Total Environment* **595**, 567–583 (2017).

198. Creber, S. A. *et al.* Magnetic resonance imaging and 3D simulation studies of biofilm accumulation and cleaning on reverse osmosis membranes. *Food and Bioproducts Processing* **88**, 401–408 (2010).

199. Leterme, S. C., Le Lan, C., Hemraj, D. A. & Ellis, A. V. The impact of diatoms on the biofouling of seawater reverse osmosis membranes in a model cross-flow system. *Desalination* **392**, 8–13 (2016).
200. Karkhanechi, H., Takagi, R. & Matsuyama, H. Biofouling resistance of reverse osmosis membrane modified with polydopamine. *Desalination* **336**, 87–96 (2014).
201. Yu, W., Yang, Y. & Graham, N. Evaluation of ferrate as a coagulant aid/oxidant pretreatment for mitigating submerged ultrafiltration membrane fouling in drinking water treatment. *Chemical Engineering Journal* **298**, 234–242 (2016).
202. Cho, J., Amy, G. & Pellegrino, J. Membrane filtration of natural organic matter: initial comparison of rejection and flux decline characteristics with ultrafiltration and nanofiltration membranes. *Water Res* **33**, 2517–2526 (1999).
203. Jeong, S., Naidu, G., Vollprecht, R., Leiknes, T. O. & Vigneswaran, S. In-depth analyses of organic matters in a full-scale seawater desalination plant and an autopsy of reverse osmosis membrane. *Sep Purif Technol* **162**, 171–179 (2016).
204. Zhu, X. & Elimelech, M. Colloidal Fouling of Reverse Osmosis Membranes: Measurements and Fouling Mechanisms. *Environ Sci Technol* **31**, 3654–3662 (1997).
205. Goh, P. S., Lau, W. J., Othman, M. H. D. & Ismail, A. F. Membrane fouling in desalination and its mitigation strategies. *Desalination* **425**, 130–155 (2018).
206. Alizadeh Tabatabai, S. A., Schippers, J. C. & Kennedy, M. D. Effect of coagulation on fouling potential and removal of algal organic matter in ultrafiltration pretreatment to seawater reverse osmosis. *Water Res* **59**, 283–294 (2014).
207. Varin, K. J., Lin, N. H. & Cohen, Y. Biofouling and cleaning effectiveness of surface nanostructured reverse osmosis membranes. *J Memb Sci* **446**, 472–481 (2013).
208. Qin, J. J., Oo, M. H., Kekre, K. A. & Liberman, B. Development of novel backwash cleaning technique for reverse osmosis in reclamation of secondary effluent. *J Memb Sci* **346**, 8–14 (2010).
209. Jee, K. Y., Shin, D. H. & Lee, Y. T. Surface modification of polyamide RO membrane for improved fouling resistance. *Desalination* **394**, 131–137 (2016).
210. Gekas, V. & Hallström, B. Mass transfer in the membrane concentration polarization layer under turbulent cross flow : I. Critical literature review and adaptation of existing sherwood correlations to membrane operations. *J Memb Sci* **30**, 153–170 (1987).
211. Hoek, E. M. V, Kim, A. S. & Elimelech, M. Influence of Crossflow Membrane Filter Geometry and Shear Rate on Colloidal Fouling in Reverse Osmosis and Nanofiltration Separations. *Environ Eng Sci* **19**, 357–372 (2002).
212. Gao, Y., Wang, Y. N., Li, W. & Tang, C. Y. Characterization of internal and external concentration polarizations during forward osmosis processes. *Desalination* **338**, 65–73 (2014).